Ph.D. Dissertation of Medicine

Prognostic use of non-invasive imaging for tumor-associated macrophages under anti-PD1 treatment

종양 관련 큰포식세포의 비침습적 영상을 통한 anti-PD1 치료의 예후 확인

February 2023

Seoul National University College of Medicine
Microbiology and Immunology

Gyo Jeong Gu

Prognostic use of non-invasive imaging for tumor-associated macrophages under anti-PD1 treatment

Doctoral advisor: Professor Seung Hyeok Seok

Submitting a Ph.D. Dissertation of Medicine

October 2022

Seoul National University College of Medicine
Microbiology and Immunology

Gyo Jeong Gu

Confirming the Ph.D. Dissertation written by
Gyo Jeong Gu
January 2023

Chair _____(Seal)

Vice Chair _____(Seal)

Examiner _____(Seal)

Examiner _____(Seal)

Examiner _____(Seal)

Prognostic use of non-invasive imaging for tumor-associated macrophages under anti-PD1 treatment

지도 교수 석 승 혁

이 논문을 의학박사 학위논문으로 제출함

2022년 10월

서울대학교 대학원

의학과 미생물학 전공

구 교 정

구교정의 의학박사 학위논문을 인준함

2023년 1월

위 원 장 _____ (인)

부위원장 _____ (인)

위 원 _____ (인)

위 원 _____ (인)

위 원 _____ (인)

ABSTRACT

Prognostic use of non-invasive imaging for tumor-associated macrophages under anti-PD1 treatment

Gyo Jeong Gu

The Department of Microbiology and Immunology

The Graduate School

Seoul National University

Since immune checkpoint inhibitors (ICIs) such as anti-programmed cell death protein 1 (PD1) inhibit tumor growth by reinvigorating the host immune system, determining their efficacy only by the changes in tumor size may prove inaccurate. Among the immune cells present in the tumor microenvironment (TME), Macrophages are abundant and critical for regulate immune responses in both innate and adaptive immunity. In this study, I aimed to investigate the dynamics of the tumor-associated macrophages (TAMs) non-invasively to confirm the response of ICI therapy. Here I performed positron emission tomography (PET) imaging during anti-PD1 treatment using mannosylated-serum albumin (MSA) labeled with radioactive isotope ^{68}Ga, which targets the mannose receptors on macrophages. Through non-invasive MSA imaging, I found an increased number of TAMs and observed that they were localized at the core of the tumor in responders. In addition, I also performed flow cytometry and PCR analyses to confirm the role of TAMs on T cells, the direct target cell of ICI therapy. I was able to demonstrate increased

frequency of TAMs produced *Cxcl9* and *Cxcl10* to recruit T cells and *iNos*, a T cell activator in responders. Although T cells are directly targeted by ICIs, it was confirmed that their activation is controlled by macrophages through co-culture of macrophages and T cells. These studies thus suggest the non-invasive imaging of TAMs can help estimate the progression of the anti-tumor response to anti-PD1 and may inform better decisions on treatment options for patients.

Keywords: Tumor-associated macrophages, Mannosylated-serum albumin, Anti-PD1, PET imaging

CONTENTS

LIST of TABLES AND FIGURES

LIST OF ABBREVIATIONS

Arginase 1: Arginase 1

BMDM: Bone marrow-derived macrophage

DSS: Dextran sodium sulfate

FDG: Fluorodeoxyglucose

FBS: Fetal bovine serum

GM-CSF: Granulocyte macrophage colony stimulating factor

HBSS: Hank's balanced salt solution

ICIs: Immune checkpoint inhibitor

M-CSF: Macrophage colony stimulating factor

MDSCs: Myeloid-derived suppressor cells

MSA: Mannosylated- serum albumin

NK cells: Natural killer cells

PD1: Programmed cell death protein 1

PD-L1: Programmed death-ligand 1

PET: Positron emission tomography

PS: Penicillin/streptomycin

RT-PCR: Real-time polymerase chain reaction

TAM: Tumor-associated macrophage

TME: Tumor microenvironment

TES: Tumor explant supernatant

WT: Wild-type

INTRODUCTION

Immune checkpoint inhibitors (ICIs) that block the programmed cell death protein 1 (PD-1)/Programmed death-ligand 1 (PD-L1) axis exert their anti-tumoral effects by reinvigorating T cells within the tumor microenvironment (TME) (1). Although ICIs can induce sustained responses, only a small portion of patients are responsive to the treatments (2). In addition, the responsiveness to ICI therapy is more challenging to assess than the traditional cytotoxic therapy, as ICIs activate immune cells to kill tumor cells rather than directly inhibiting tumor growth. Moreover, the determination of the efficacy of ICI therapy through tumor size alone is difficult due to pseudo-progression, a temporary increase in tumor size resulting from an increased infiltration of immune cells into the tumor in responders (3, 4). For these reasons, in 2017 the Response evaluation criteria in solid tumor (RECIST) working group published a modified set of response criteria, iRECIST(immune RECIST), for immunotherapy, based on RECIST 1.1 which was developed for cytotoxic therapies and adapted for targeted agents (5). However, these criteria require a consecutive scan at least 4 weeks apart for the confirmation of progressive. When the treatment is found ineffective, patients may lose the opportunity to receive other treatments during the assessing time. Therefore, determining the therapeutic effects of ICIs using mechanism-based biomarkers such as non-invasive visualization of immune cells is highly desirable.

Most of the studies related to the responsiveness of anti-PD1 therapy have focused on $CD8^+$ T cells, which can kill tumor cells directly (6, 7). These studies examined numerical increases or changes in the distribution of $CD8^+$ T cells in tumors to

interpret the therapeutic response to treatment and confirmed the levels of T cell-secreted cytokines IFNγ and Granzyme B as non-invasive indicators of immune response activation (8-11). However, there is a limitation in that the amount of labels at the site has appeared disparate from the actual cell numbers since the cell expansion and loss of cytokine activity (12). In addition, most of these studies use immune-positron emission tomography (immunoPET), which is a molecular imaging modality combining the high sensitivity of PET with the specific targeting ability of monoclonal antibodies. ImmunoPET also has some obstacles, including the high costs, advanced technology to commercially produce pure mAbs, difficulties in conjugation and stability, high circulation time, and physiologic uptake after administration (13) .

Tumor-associated macrophages (TAMs) are the most abundant immune cells of the TME in solid tumors (14). They display remarkable heterogeneity and plasticity depending on the TME, as well as highly correlated with ICI therapeutic efficacy (14-16). TAMs are widely known as one of the essential myeloid cells in establishing immunosuppressive TMEs, along with myeloid-derived suppressor cells (MDSCs) and regulatory T cells (Tregs) (17). TAM-mediated immunosuppressive niches impair T cell boosting and contribute to resistance to ICI therapy (18-20). Some studies identified that impeding $CD8^+$ T cells from the tumor was modulated by TAMs and limiting ICI therapy's effects. Further, intravital live imaging showed that $PD1^-$TAMs capture and retain anti-PD1 from $CD8^+$ T cell surfaces, thus negating the impact of the treatment (21). On the contrary, it was observed that the depletion of TAM abrogated the effects of the anti-PD1 therapy (22). Moreover, recent studies identified an inflammatory $Cxcl9^+MHCII^+CD40^+$ TAM population that correlates

with responses to avelumab (23). However, non-invasive monitoring of TAMs after therapy has not been investigated, despite their ability to modulate T cell activation and control immune responses after ICI therapy. Therefore, longitudinally monitoring the changes in TAMs during ICI therapy could expand our understanding of the therapeutic effects of ICIs and yield a more accurate prediction of the therapy response.

ICI therapy induces a complex network of secreted signals in TMEs. This therapy-induced secretome (TIS) stimulates the outgrowth, dissemination, and metastasis of cancer cell, contributing to incomplete tumor regression (24). Especially, secreted proteins (cytokines and chemokines) derived from the TIS are a major factor in influencing the differentiation of monocytes to TAMs. Monocyte chemoattractant protein-1 (MCP-1, also known as CCL2) is a strong recruiter of monocytes to the tumour (25). Prostaglandin E2 (PGE2) and colony-stimulating factor 1 (CSF1), from therapy-treated cancer cells, can skew monocyte differentiation to a more M2-like macrophage expressing IL-10 and influence TAMs to support tumour survival and regrowth post chemotherapy by enhancing tumour cell autophagy (26, 27). Nevertheless, it is critical that re-educated TAMs by TIS are modulates the relapse or promote anti-tumour immunity through modulation of T cells. Therefore, it is necessary to understand how macrophages and T cells were affected by TME according to anti-PD1 responsiveness.

In this study, I used ^{68}Ga-labeled mannosylated- serum albumin (MSA) to trace TAMs non-invasively after anti-PD1 treatment. MSA nanoparticle was developed as a macrophage-specific tracer by binding to a mannose receptor (CD206) expressed by macrophage (28). In previous studies, [^{68}Ga]Ga-MSA PET imaging can help

diagnose pulmonary artery hypertension and monitor the inflammatory status by imaging the degree of mannose receptor-positive macrophage infiltration into the lung (29). In addition, [^{68}Ga]Ga-MSA PET imaging also visualizes the infiltration of mannose receptor-positive macrophages in monitoring myocarditis's treatment response (30). Through these studies, I assumed that the [^{68}Ga]Ga-MSA PET imaging could be a novel noninvasive diagnostic and monitoring tool for mannose receptor-positive TAM after immunotherapy.

Based on the optimized MSA nanoparticle imaging, I confirmed that the CD206 expressing TAMs were increased in the anti-PD1 responder and moved into the tumor's core in B16F10 and MC38 mouse models. Of note, I evaluated the anti-tumoral immune status of TME using FACS analysis of T cell activity. I further revealed that TAMs induce the movement of $CD8^+$ T cells into the tumor core through the secretion of chemokines and regulate the proliferation of $CD8^+$ T cells. These results suggest that monitoring TAMs as biomarkers can help predict the response to ICI therapy and improve its efficacy.

MATERIALS AND METHODS

Ethics approval

Animal experiments were conducted in accordance with the Institute for Experimental Animals, College of Medicine, and were performed according to the Guide for the Care and Use of Laboratory Animals prepared by the Institutional Animal Care and Use Committee of Seoul National University (accession number: SNU-150108-3-3, SNU-190930-6-8).

Cell lines and cell culture

The B16F10 murine melanoma-derived cell line was purchased from the ATCC (CRL-6475, Manassas, VA, USA) and cultured in RPMI 1640 medium (Gibco, Carlsbad, CA, USA) containing 10 % fetal bovine serum (FBS, Gibco) and 1 % penicillin/streptomycin (PS, Gibco) at 37 °C in a humidified incubator containing 5 % CO_2. Murine colon adenocarcinoma MC38 cell line was given by Prof. Nam hyuk Cho. Cells were maintained in Dulbecco's modified essential medium (Gibco) supplemented with 10% FBS and 1 % at 37 °C in a humidified incubator containing 5 % CO_2

Mice and tumor models

Seven to ten-weeks-old wild-type (WT) C57BL/6 female mice were used in all the experiments. B16F10-luciferase expressing (B16F10-Luc) cells and MC38-Luciferase expressing (MC38-Luc) cells were used in all experiments. B16F10-Luc (3×10^5) cells and MC38-Luc (3×10^5) cells were injected into the left and right

flanks. Tumor volume was calculated by using formula (width^2 × length) /2 every 3–4 d. After tumor implantation, 100 μg anti-PD1 (clone 29F.1A12, BioXcell, USA) was administered three times. Animals that did not grow tumors or had tumors smaller than 5 mm in diameter on the first day of anti-PD1 treatment were excluded. The response was determined by comparing tumor volume change at time t to its baseline:% tumor volume change = ΔVol_t = 100% × (($V_t - V_{initial}$) / $V_{initial}$). For each time t, the average of ΔVol_t from t = 10 to 25 was calculated and defined as the BestAvgResponse. After the last imaging, the tumors were collected for histology, flow cytometry, and PCR analysis.

Colitis model and [^{18}F]-FDG PET imaging

Seven to ten-weeks-old wild-type (WT) C57BL/6 male mice were provided with water containing 3% dextran sodium sulfate (DSS; MP Biomedicals, Santa Ana, California, USA) for 6 d to induce colitis. [18F]-FDG synthesis was performed at the Seoul National University Hospital Cyclotron Facility. Mice were fasted for at least 6–8 h before [18F]-FDG injection and anesthetized with 1.5% isoflurane throughout 60-min uptake and during image acquisition. All PET images were acquired with a Genesis4 small-animal PET/X-Ray scanner (Sofie Biosciences, Culver City, CA, USA). Three-dimensional PET data were acquired from whole body approximately 60 min after i.v. administration of 30 μCi of [18F]-FDG per mouse for 3 min. After imaging, colon lamina propria cells were isolated for quantifying FDG uptake of macrophages. A total of 105 cells of the CD45+F4/80+ population was sorted using FACS Aria III (BD Biosciences) and analyzed by a glucose uptake fluorometric assay kit (BioVision, Milpitas, California, USA).

Immunohistochemistry

Immunohistochemistry was performed according to the manufacturer's instructions. Briefly, paraffin-embedded sections were deparaffinized, hydrated, and antigen retrieved by steaming the slides in sodium citrate buffer (10 mM sodium citrate, pH 6.0). The slides were then treated with 3 % H_2O_2 and blocked using a blocking solution. Primary antibodies were pre-diluted in blocking solution at 1:200 for CD206 (R&D Systems, Minneapolis, MN, USA) and applied to tissue sections overnight at 4 °C in a humidified chamber. Biotinylated secondary antibodies were then applied, followed by signal development using liquid DAB substrate (Dako, Glostrup, Denmark). Sections were counterstained with hematoxylin (Abcam, Cambridge, UK). The slides were scanned using a digital camera Aperio AT2 (Leica, Wetzlar, Germany). Analysis of immunohistochemistry staining intensity was performed using ImageJ through IHC profiler plugin.

Flow cytometry

The s.c. tumors were minced and then digested in HBSS - 10% fetal bovine serum containing 2mg/ml collagenase type I (Sigma Aldrich, St. Louis, MA, USA) and 10 μg/ml DNase I (Sigma Aldrich) at 37 °C for 30 min to digestion. Digested cells were passed through a 70 μm pore size cell strainer to prepare single cell suspensions for flow cytometry. Anti-mouse CD16/32 antibody (93, BioLegend, San Diego, California, USA) was pre-added to block the non-specific binding of the immunoglobulin to macrophage Fc receptors. For surface marker analysis, live cells were re-suspended in FACS buffer (1 % BSA, 0.1 % sodium azide in PBS) and

stained with anti-mouse CD45 (30-F11), F4/80 (BM8), Ly6C (HK1.4), CD11b (M1/70, eBioscience, San Diego, California, USA), Ly6G (RB6-8C5, BioLegend), CD206 (MR6F3), CD3 (145-2C11), CD8α (53-6.7), and CD4 (RM4-5) (eBioscience) at 4 °C for 20 min. For intracellular staining, cells were incubated for 2 hours with GolgiPlug (BD Biosciences, Franklin Lakes, New Jersey, USA) and GolgiSTOP (BD Biosciences) at 1 μl/ml of culture media. Cells were then surface stained and then fixed and permeabilized using Foxp 3 staining Buffer (Invitrogen, Waltham, Massachusetts, USA), the labeled with Granzyme B (NGZB, eBioscience) and IFN-γ (XMG1.2, BD Biosciences). Data were acquired using an LSRFortessa system (BD Biosciences) and analyzed with FlowJo software version 10.8.1. (BD Biosciences).

Immunofluorescence

Mouse tumor tissues were embedded in optimal cutting temperature (OCT) compound, frozen and stored at −80 °C. Frozen samples from these tissues were fixed in 4% paraformaldehyde for 15 min and washed with PBS, then blocked with PBS containing 3% bovine serum albumin (BSA) and 0.3% Triton X-100 (Sigma-Aldrich) for 1 h at room temperature. Tissue sections were then rinsed in staining buffer (1% BSA and 0.3% Triton X-100 in PBS) and incubated overnight at 4°C with primary antibodies (anti-CD206; Abcam, anti-CD8; Thermo Fisher Scientific, anti-F4/80; BioRad) diluted in PBS containing 1% BSA and 0.3% Triton X-100. After washing with PBS thrice, the tissue sections were stained with the appropriate secondary antibodies and 4,6-diamidino-2-phenylindole (DAPI; Invitrogen) for 1 h. Staining controls were stained with secondary fluorescently labelled antibodies and DAPI without primary antibodies. To detect apoptotic cells in tumor sections,

cryopreserved sections were stained with an In Situ Cell Death Detection Kit (Roche, Basel, Switzerland) according to the manufacturer's protocol. Fluorescent images were acquired on a Leica TCS SP8 confocal microscope (Wetzlar).

Quantitative Real-time PCR

Total RNA was extracted from the tumor and TES educated macrophages using TRIzol reagent (Invitrogen) according to the manufacturer's instructions. cDNA was reverse transcribed from 1 mg of total RNA, and the amount of mRNA was determined by real-time PCR using the SYBR Green qPCR Pre-Mix (Enzynomics, Daejeon, South Korea). All samples were normalized to the 18S rRNA mRNA expression levels. The primer sequences are listed in Table I.

Isolation of primary macrophage and preparation of tumor explant supernatant (TES)

Primary macrophages were differentiated from mouse bone marrow cells. Bone marrow cells were obtained from 7-10-week-old C57BL/6 male mice and differentiated into mature bone marrow-derived macrophages (BMDMs) for 7 d in RPMI 1640 containing 10 % FBS, 1 %, and 2 mM L-glutamine (Gibco) supplemented with fresh recombinant murine macrophage-colony stimulating factor (M-CSF) (50 ng/ml; Miltenyi Biotec, Bergisch Gladbach, Germany). The medium was replaced on days 3 and 5 with a fresh medium containing M-CSF. For preparing TES, tumors from B16F10-bearing mice were dissected and minced using a blade in a cell culture plate (1 g tumor/15 mL RPMI media). After chopping, tumors were incubated in a humidified incubator at 37 °C with 5 % CO_2. Supernatants were

collected after 24 h. To remove the debris, the supernatant was centrifuged at 12,000 × g and filtered using a 0.2 μm pore size syringe filter.

T cell proliferation assay

Splenocytes isolated from fresh mouse spleen tissue were labeled with the CellTrace Violet dye (Thermo Fisher Scientific, Waltham, Massachusetts, USA) according to the to manufacturer's instructions. The labeled cells were seeded in 96-well round-bottom plates at 5 x 10^5 cells/mL and then incubated for 96 h with TES from tumors supplemented with anti- CD3/CD28 (Thermo Fisher Scientific). For co-culture, labeled cells were co-cultured with BMDMs (1:5 ratio of BMDMs to T cells) in RPMI 1640 medium supplemented with 10% FBS and anti- CD3/CD28. After 96 h at 37 °C, cells were stained with CD4 PE (GK1.5; eBioscience) and CD8a APC-Cy7 (53.6.7; BioLegend) for 30 min at 4 °C. T cell proliferation was determined by Cell Trace Violet dye and analysis with flow cytometry.

Synthesis of [^{68}Ga]Ga-mannosylated- serum albumin (MSA)

For synthesizing [^{68}Ga]Ga-MSA using click chemistry, we used a modified method described in our previous report.(25, 26) Briefly, albumin (50 mg, 757 nmol) in phosphate buffered saline (PBS, 0.5 mL, pH 7.4) was reacted with azadibenzocyclooctyne-PEG4-N-hydroxysuccinimidyl ester (ADIBO-NHS, 4 mg, 8.4 μmol) in DMSO (10 μL). The reaction mixture was kept at 4 °C for 4 h and purified using a centrifugal filter unit (30 kDa) to form ADIBO-albumin (42 mg, 6.05 nmol). The number of ADIBO groups on albumin was determined to be 9.3 by matrix-assisted laser desorption/ionization-time of flight (MALDI-TOF). Mannosyl

groups on albumin were introduced by a click reaction with ADIBO-albumin and azido-mannose (Man-N_3). Man-N_3 (1.6 mg, 4.8 μmol) in PBS (100 μL) was added to ADIBO-albumin (42 mg, 6.05 nmol) in PBS (100 μL), and the reaction mixture was kept at 4 °C for 2 h and purified using a desalting column (PD-10) with PBS as an eluent to yield mannosylated- serum albumin (MSA, 39.9 mg, 588 nmol). The number of mannosyl groups on albumin was determined using MALDI-TOF to be 6.6. The size of ADIBO-albumin and MSA was measured as 7.101±1.021 nm and 8.534±1.224 nm, respectively, using dynamic light scattering. MSA was then labeled with fluorescent dyes (FL) and radioisotopes in the residual ADIBO groups. For fluorescence labeling, MSA (588 nmol/0.5 mL PBS) was reacted with FNR648-N^3 (44 μg, 58 nmol) in DMSO (6 μL) for 30 min. The reaction mixture was purified using a centrifugal filter (30 kDa) and concentrated to yield fluorescence-labeled MSA (MSA-FL, 500 nmol/0.5 mL in PBS). Lastly, MSA-FL was radiolabeled with gallium-68 (^{68}Ga, half-life: 68 min). For radiolabeling, 3-azidopropyl-NOTA (NOTA-N3, 10 μg, 18 nmol) in 0.1 M sodium acetate buffer (pH 5.5, 1 mL) was mixed with freshly eluted ^{68}Ga (370 mBq) in 0.1 M HCl solution (1 mL) to give [^{68}Ga]Ga-NOTA-N_3 with quantitative yield. MSA-FL (7.1 mg, 100 nmol) was then reacted with [^{68}Ga]Ga-NOTA-N3 (37 MBq/200 μL) to yield radiolabeled MSA-FL ([^{68}Ga]Ga-MSA) with quantitative yield. After radiolabeling, [^{68}Ga]Ga-MSA was used for PET imaging without further purification. The radiochemical purity of [^{68}Ga]Ga-MSA was > 99 % and the Rf values of the free ^{68}Ga, [^{68}Ga]Ga-NOTA-N_3, and [^{68}Ga]Ga-MSA were 0.9–1.0, 0.7–0.8, and 0.0–0.1, respectively, in radio-TLC.

PET image acquisition and analysis

A small animal PET system (Genisys PET box, Sofie Biosciences, California, USA) was used for PET acquisition for 5 min 2 h after injection. The activity of the injected [^{68}Ga]Ga-MSA was 50 μCi/0.1mL. Reconstruction of the PET images was automatically performed using vendor-provided software. The [^{68}Ga]Ga-MSA of each tumor was assessed by a semi-quantitative method using LifeX software version 7.0.15. The maximum counts of tumors were measured using manual volumes-of-interest placed on the tumor lesions. For count normalization, another manual spherical volume-of-interest was placed on the mediastinum to reflect blood pool counts. Tumor uptake was represented by the maximum lesion-to-blood pool (LBP) ratio as a measurement of the [^{68}Ga]Ga-MSA uptake.

Statistical analysis

All statistical analyses were conducted using GraphPad Prism software (version 8.0) and are displayed as the mean ± S.E.M. Statistical significance was assessed using Student's t-test, and ANOVA with Tukey's post-test was performed for multiple comparisons.

RESULTS

Effective anti-PD1 treatment drives augmented TAM infiltration along with increased $CD8^+$ T cell abundance and activity in the complete response model.

Before the confirm the change of TAMs non-invasively according to anti-PD1 responsiveness, I first investigated the infiltration of macrophages and T cells in the B16F10 model. After inoculation with B16F10-Luc melanoma cells (3×10^5, s.c., upper right flank), mice were treated with 200 μg of anti-PD1 four times every 3 d **(Figure 1A).** By anti-PD1 treatment, B16F10 tumor growth was significantly reduced to be classified as a responder group **(Figures 1B and C).** In this model, I first explored activations of $CD8^+$ T cells, which directly target of the anti-PD1. As expected, I observed an increased number of $CD45^+$ immune cells and $CD3^+$ T cells **(Figures 2A – C)**. In addition, the enhanced anti-tumor activity of CD8+ T cells was also confirmed in the anti-PD1 treatment group **(Figure 2D).** These results indicate that the anti-PD1 treatment group is the reinvigoration of T cells. I next evaluated the remodeling of TAMs following anti-PD1 treatment. As I expected, the anti-PD1 treatment promotes the recruitment of TAMs **(Figure 3A).** However, the population of $CD11b^+F4/80^+CD206^+$ (traditionally recognized as immunosuppressive phenotype) macrophages was also augmented following anti-PD1 treatment **(Figure 3B)**. In previous references, it has also been known that the $CD11b^+F4/80^+MHCII^+$ (traditionally recognized as activated phenotype) macrophages were increased in anti-PD1 treatment. I observed that the expression of MHCII was higher in the anti-PD1 treatment group **(Figure 3C)**. I also confirmed that CD206 expressing TMAs were low in the anti-PD1 treatment group through $MHCII^-$ cell gating **(Figure 3D)**.

To further define the phenotype of TAMs, I confirm the expression of Arginase and iNOS. iNOS expressing TAMs were increased, and Arginase-1 expressing TAMs were decreased in the anti-PD1 treatment group **(Figure 3E)**. Finally, I confirmed the CD206-expressing cells were increased entirely in the anti-PD1 treatment group in this model **(Figures 3F and G)**. Collectively, these findings led to a change in my hypothesis. This is because I thought there would be fewer $CD206^{+}$ cells in the anti-PD1 treatment group than control. The above results indicate that macrophages expressing CD206 in the tumor may augment the anti-PD1 treatment.

The establishment of a cohort model for responders and non-responders of anti-PD1 treatment.

I established an experimental model randomly responding to anti-PD1 treatment to obtain a more variable response. After inoculation with B16F10-Luc melanoma cells (3×10^5, s.c., upper left and right flank), mice were treated with 100 μg of anti-PD1 three times every 4 d. In this setting, the ratio of responders to non-responders was approximately 4:6. I first confirmed that the tumor size and weight were reduced in the responder group **(Figures 4A and B)**. To evaluate the anti-PD1 response in this model, I used modified RECIST criteria **(Table 2)** (31). Based on these criteria, I divided the responder and non-responders **(Figure 4C)**. In serial tumor volume, I observed evidence of pseudo-progression, where ICI therapy induced an initial increased of the measurable tumor between d 10 and d 18 followed by a rapid regression between d 18 and d 28 in 66.6 % of responders mice, while only 33.3 % of responder mice showed immediate lesion regression between d 10 and d 18 **(Figure 4A)** (32). Next, I investigated the differences in myeloid cells infiltrating

the tumors between non-responders and responders. Consistent with my previous data, infiltration of $CD45^+$ cells increased in response to anti-PD1 treatment **(Figure 5A)**.

Further detailed analyses of infiltrated $CD45^+$ cells revealed that, aside from lymphoid cells, including $CD8^+$ T cells, the most significant increase was observed in TAMs **(Figure 5B and Figure 6)**. In addition, I observed that the presence of granzyme B^+ and $IFN\gamma^+$ staining in $CD8^+$ T cells from responders was increased **(Figure 7A)**. To understand why T cell infiltration is raised, I examined the expression of *Cxcl9* and *Cxcl10*, which are essential chemoattractants of T cells (33). *Cxcl9* and *Cxcl10* expression was higher in responder than in non-responder tumors **(Figure 7B)**. Tumor-draining lymph nodes (TdLNs) are essential to prime the anti-tumor lymphocytes for tumor-specific antigens and play pivotal roles in immune responses against tumors. I obtained TdLNs and conducted analysis of T cell components. As I expected, $CD8^+$ T cells were increased and Foxp3+ T regs were decreased in responder TdLN **(Figures 8A and B)** Collectively, these results show that my random response model is well-established with previously reported features.

[^{68}Ga]Ga-MSA-PET imaging shows different tumor-associated macrophage states in response to anti-PD1 treatment

Mannosylated-serum albumin (MSA) is a small molecule that binds to a mannose receptor and has been developed as a tracer targeting the mannose receptor (CD206) of macrophages **(Figure 9A)** (34). Prof. Yoon-sang Lee provided the MSA, and I used it in this experiment.

Although previous studies have already confirmed that MSA can target CD206 of

TAMs, I have once again checked whether MSA can target CD206 of TAMs before *in vivo* experiments. To induces the expression of CD206 on the macrophages, I treated IL-4 to the BMDM for 24 hr. after that, the MSA and non-targeted serum albumin (SA) were treated to the CD206 expressing macrophages. As a result, most of the CD206 expressing cells uptake the MSA. but unexpectedly, a considerable amount of the non-targeted SA was also uptake. This result suggests a receptor-independent uptake due to the phagocytic activity of the macrophages. However, I confirmed that the reduced uptake of MSA by about 20 % when I used manna to block the expression of CD206 **(Figure 9B)**. The *in vitro* experiment had a limitation in confirming the specificity of MSA. Next, I confirmed the colocalization of CD206 and MSA in the tumor tissue *in vivo* **(Figure 9C)**. Moreover, most CD206-expressing cells were macrophages, F4/80 positive cells **(Figure 9D)**. To determine whether MSA nanoparticles are binding on TAM, I performed additional analysis of flowcytometry data in my experiment. I confirmed that about 88% of most MSA^+ cells were $CD11b^+F4/80^+$ cells (**Figure 9E**). Collectively, I showed the CD206 expression among the intra-tumoral total cells like signal of [^{68}Ga] Ga-MSA in the tumor.

TAMs are generally expressed mannose receptors. However, it is not well known why the expression of mannose receptors is induced and the role of mannose receptors in tumors. Before I conducted the TAMs imaging in the anti-PD1 treated mice, I confirmed that the TAMs significantly increased CD206 expression in anti-PD1 treated tumors **(Figures 10A, B and C)**. I conducted RT-PCR to confirm a shift in chemokines related to macrophage recruitment, *Ccl2,* and *Ccl5*, suggesting the enhanced recruitment of macrophages **(Figure 10C)**. Additionally, quantifying

CD206 stained tumor tissue showed that the number of $CD206^+$ cells increased at the tumor core in the responder compared to the non-responder **(Figure 10D)**.

Next, I explore whether [^{68}Ga]Ga-MSA could non-invasively detect the infiltration of CD206-expressing TAMs according to anti-PD1 reactivity. I conducted PET imaging two hours after administration of [^{68}Ga]Ga-MSA on days 15 and 24. Furthermore, I examined the location of these immune cells in the tumor. Interestingly, I observed that the [^{68}Ga]Ga-MSA signal appeared evenly throughout the tumor in responders but only at the tumor margin in the non-responders **(Figure 11A)**. Upon quantitative measurement, the maximum LBP ratio of the responders was significantly higher than that of non-responders **(Figure 11B)**. In line with [^{68}Ga]Ga-MSA PET imaging, further analysis confirmed increased MSA uptake in the responder tumors, albeit with a very small size **(Figure 11C)**. I thus found that tumor size and the degree of [^{68}Ga]Ga-MSA uptake showed a negative correlation **(Figure 11D)**.

Consistent with the anti-PD1-response of B16F10, higher frequencies of $CD206^+$ cells were observed in responders of MC38 models (**Figures 12A and B**); furthermore, the [^{68}Ga]Ga-MSA signal of the responders was higher than non-responders and appeared throughout the (**Figures 12C and D**).

After then, I wondered about [^{18}F]-FDG-PET imaging on the anti-PD1 random response model. I tested whether the responsiveness could be determined only by the [^{18}F]-FDG-PET imaging in the cancer model. Although [^{18}F]-FDG uptake is as sociated with elevated glycolysis in cancer cells, it can also be related to infla mmation or immune reactions due to the consumption of glucose by immune c ells. As I expected, [^{18}F]-FDG PET imaging did not indicate the difference betw

een responder and non-responders in the B16F10 model (**Figure 13**).

ICI therapy also induces the activation of immune cells, which is an inflam mation [^{18}F]-FDG-PET imaging is insufficient to discriminate the responsivenes s to anti-PD1. Because in my previous experiments (35), I found that GM-CSF induces macrophage phenotype to inflammation through up-regulating the glyco lytic capacity. I conducted [^{18}F]-FDG-PET experiment to confirm the high glyc olytic activity of inflammatory macrophages during colitis. PET images showed increased FDG uptake for both the small intestine and the large intestine of th e DSS-induced colitis group and low FDG uptake in normal mice. FDG uptake of GM-CSF neutralizing Ab–treated colitis mice showed reduced uptake compa red with isotype-treated colitis mice (**Figure 14A**). Next, to more precisely define the involvement of macrophages *in vivo*, I examined GLUT1 expression of CD45$^+$ F4/80$^+$ CD11b$^+$ colonic lamina propria macrophages. As expected, colonic macrophages from DSS-induced inflamed mice showed increased GLUT-1 expression compared with naive mice, and GM-CSF neutralization completely inhibited GLUT-1 upregulation (**Figure 14B**). From this data, I confirmed that th e macrophage activation in the inflammatory state induces higher glucose uptak e than in the steady state. ICI therapy also induces the activation of immune c ells, which is an inflammation [^{18}F]-FDG-PET imaging is insufficient to discri minate the responsiveness to anti-PD1. Collectively, these findings demonstrate a significant difference in the frequency and location of TAMs within the TME.

The tumor microenvironment altered by anti-PD1 treatment allows macrophages to induce infiltration and activation of CD8$^+$ T cells

Next, I wondered about macrophage and T cell interaction in TME at the anti-PD1 treated tumor. Given the well-described roles of TAMs in inducing T cell activation (36-38), I investigated the effect of ICI-induced TME alteration on TAMs, which affected T cells. To do this, I prepared tumor explant supernatant (TES) from both responders and non-responders. Further, bone marrow-derived macrophages were treated with TES for 24 h, and *Cxcl9, Cxcl10,* and *il-10* mRNA expression was determined. A simplified schematic of the experiment is shown in **Figure 15A**. As expected, the expression of *Cxcl9* and *Cxcl10* was induced, but the *il-10* expression was decreased in macrophages exposed to responder-derived TES. **(Figure 15B)**.

After then, I also analyzed the capacity of macrophages for the proliferation of T cells in response to anti-PD1. First, T cell proliferation assays were performed to confirm the direct effects of TME on T cell activation. I collected TES from tumors treated with anti-PD1, and T cells purified from splenocytes were exposed to TES **(Figure 16A)**. Surprisingly, there was no difference between each other **(Figure 16B)**.

To investigate the direct influence of macrophages on $CD8^+$ T cells, I used a co-culture system with TES-educated macrophages and $CD8^+$ T cells and observed proliferative activity. When the co-culture was conducted with responder-derived TES-educated macrophages with $CD8^+$ T cells, the proliferative activity of $CD8^+$ T cells was increased **(Figures 17A and B)**, indicating the enhanced anti-tumor activity of macrophages for inducing T cell immunity. Collectively, my observations proved that increased infiltration of TAMs could promote T-cell mediated anti-tumor immune responses upon anti-PD1 treatment.

Ccl2	F: 5′-CTC CAG CCT ACT CAT TGG GAT CA-3′ R: 5′-CTC CAG CCT ACT CAT TGG GAT CA-3′
Ccl5	F: 5′-ACT CCC TGC TGC TTT GCC TAC-3′ R: 5′- ACT TGC TGG TGT AGA AAT ACT-3′
Cxcl9	F: 5′-AGC CCC AAT TGC AAC AAA AC-3′ R: 5′-TCT TCA CAT TTG CCG AGT CC-3′
Cxcl10	F: 5′-GGG CCA TAG GGA AGC TTG AA-3′ R: 5′-GGA TTC AGA CAT CTC TGC TCA TCA-3′
iNos	F: 5′-TCC TGG AGG AAG TGG GCC GAA G -3′ R: 5′-CCT CCA CGG GCC CGG TAC TC-3′
Il-1β	F: 5’-CTC AAT GGA CAG AAT ATC AAC CAA CA-3’ R: 5’-ACA GGA CAG GTA TAG ATT CTT TCC TTT G-3’
TNFα	F: 5’-CACCCCGAAGTTCAGTAGACA-3’ R: 5’- GAACTGGCAGAAGAGGCACT-3’
18SrRNA	F: 5′- GCA ATT ATT CCC CAT GAA CG -3′ R: 5′- GGC CTC ACT AAA CCA TCC AA -3′

Table 1. Primer sequences for QRT-PCR

Table 2. Criteria for response assessment of mouse model under immunotherapy based on RECIST.

Non-responder		Responder	
Stable disease (SD)	Progressive disease (PD)	Complement response (CR)	Partial response (PR)
BestAvgResponse < 30%	Neither CR, PR nor SD	BestAvgResponse < −40%	BestAvgResponse < −20%

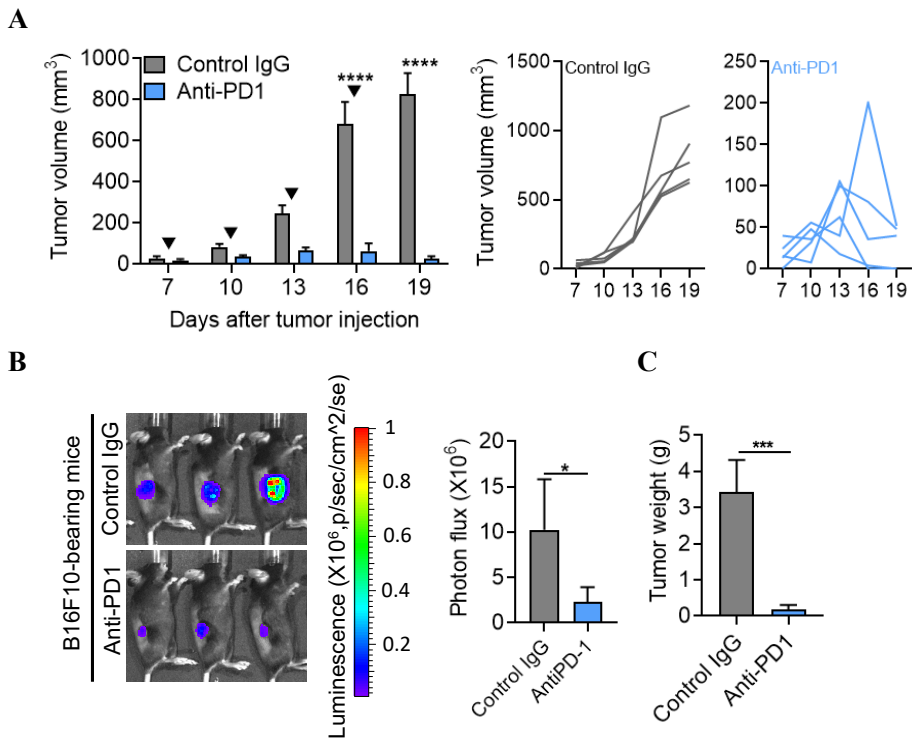

Figure 1. Complete response model to anti-PD1 treatment in a murine model of melanoma. B16F10 tumor-bearing mice were treated with 200 μg of anti-PD1(▼) on day 7, day 10, day 13, and day 16. Tumors were obtained 12 d after initiating the anti-PD1 treatment. (**A**) Average (left) and individual (right) tumor volume. **(B)** In vivo luminescence imaging of tumor-bearing mice (n = 3/group). **(C)** Tumor weight following anti-PD1 treatment in B16F10 tumor-bearing mice (n = 5/group). Data are presented as mean ± SEM. Statistical significance was determined using a two-tailed Student's *t*-test. Data shown are representative of three independent experiments performed. *$p < 0.05$; ***$p < 0.001$; ****$p < 0.0001$.

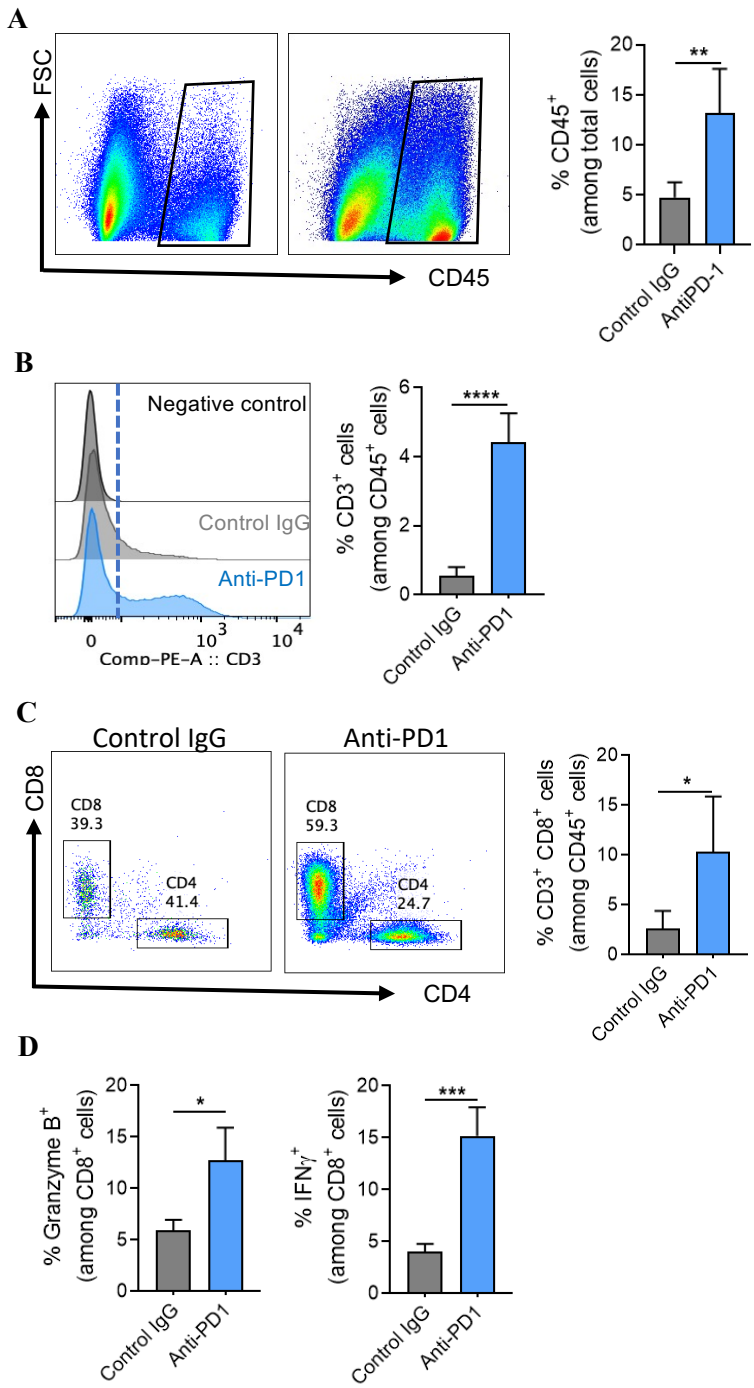

Figure 2. Increased infiltration and activation of CD8$^+$ T cells in anti-PD1 responders. (A-D) Flow cytometric quantification of tumor-infiltrating CD45$^+$ **(A),** CD3$^+$ T cells **(B),** CD8$^+$**(C),** and Granzyme B$^+$ and IFNγ^+ **(D)** in tumor infiltrating

$CD8^+$ T cells T cells (n = 5/group). Data are presented as mean ± SEM. Statistical significance was determined using a two-tailed Student's *t*-test. Data shown are representative of three independent experiments performed. *$p < 0.05$; **$p < 0.01$; ***$p < 0.001$; ****$p < 0.0001$.

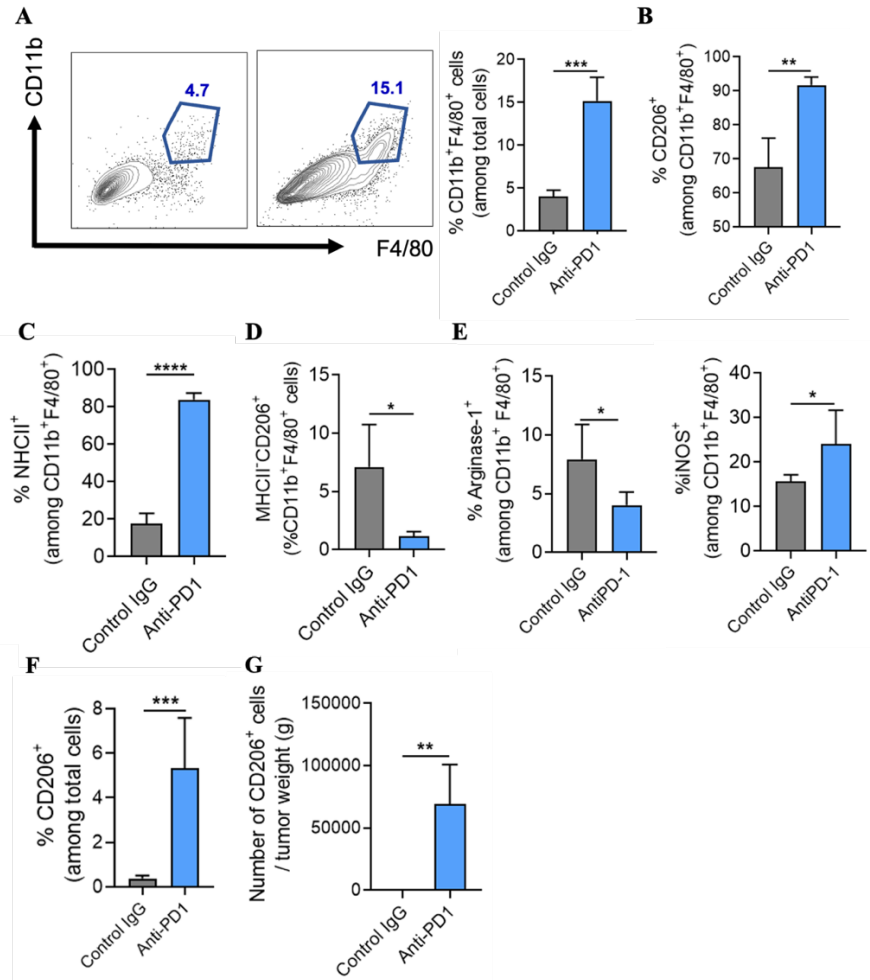

Figure 3. Anti-PD1 treatment promotes recruitment of TAMs. (A-E) Flow cytometric quantification of tumor-infiltrating $CD11b^+$, $F4/80^+$ macrophages **(A)**, $CD11b^+$, $F4/80^+$, $CD206^+$ macrophages **(B)**, $CD11b^+$, $F4/80^+$, $MHCII^+$ macrophages **(C)**, $CD11b^+$, $F4/80^+$, $MHCII^-$, $CD206^+$ macrophages **(D)**, and Arginase-1^+ and $iNOS^+$ in tumor infiltrating macrophages **(E)**. **(F)** Frequency of $CD206^+$ cells (n = 5/group). **(G)** The number of CD206+ cells normalized to tumor weight. Data are presented as mean ± SEM. Statistical significance was determined using a two-tailed Student's *t*-test. Data shown are representative of three independent experiments performed. *$p < 0.05$; **$p < 0.01$; ***$p < 0.001$.

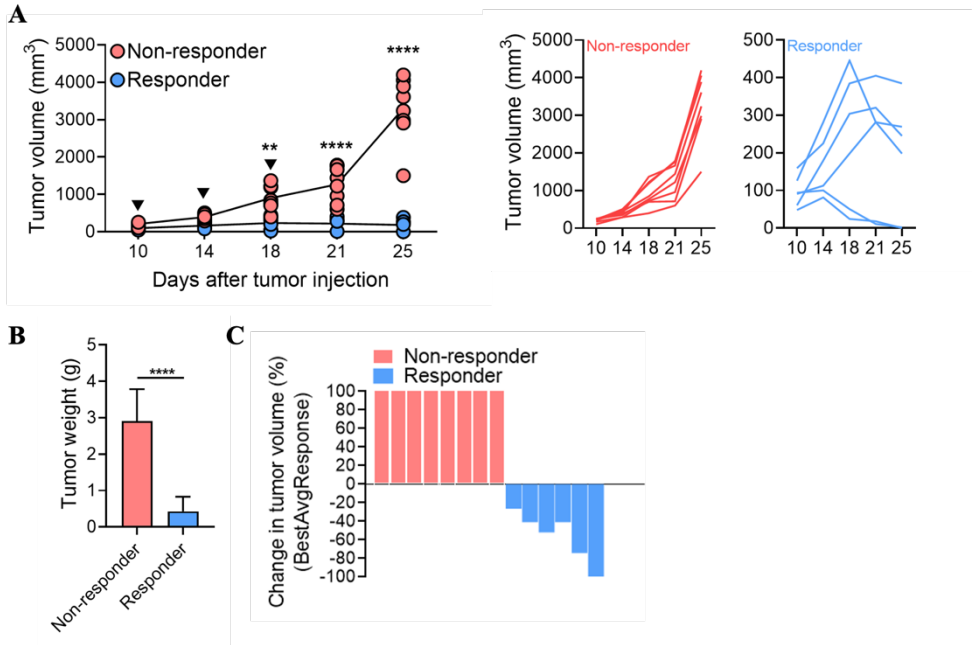

Figure 4. Establishment of random responsive model to anti-PD1 treatment in a murine model of melanoma. B16F10 tumor-bearing mice were treated with 100 μg of anti-PD1(▼) on day 10, day 14, and day 18. Tumors were obtained 15 d after initiating the anti-PD1 treatment. (**A**) Average (left) and individual (right) tumor volume and tumor weight following anti-PD1 treatment in B16F10 tumor-bearing mice (non-responders, n = 8; responders, n = 6). **(B)** Tumor weight after anti-PD1 treatment. (non-responders, n = 8; responders, n = 6). **(C)** Waterfall plot of response to anti-PD1 (non-responders, n = 8; responders, n = 6). Data are presented as mean ± SEM. Statistical significance was determined using a two-tailed Student's *t*-test. Data shown are representative of three independent experiments performed. $^{**}p < 0.01$; $^{****}p < 0.0001$.

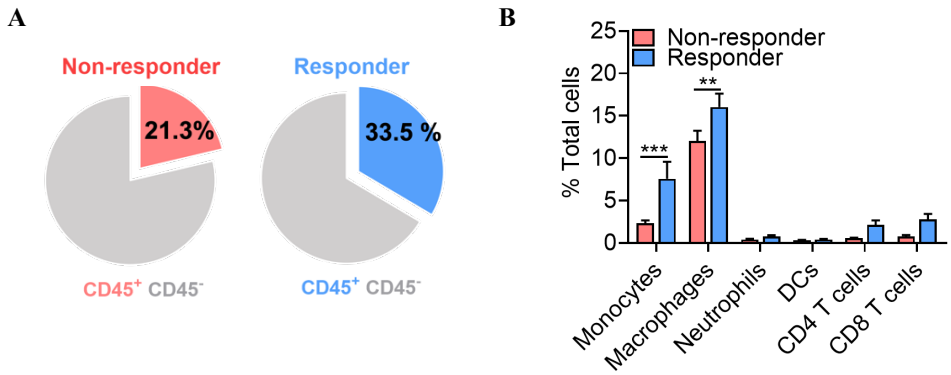

Figure 5. Augmented infiltration of immune cells in anti-PD1 Responders. (**A**) Pie chart indicating the percentage of $CD45^+$ and $CD45^-$ cells in non-responder and responder tumors at day 15 after anti-PD1 treatment. (**B**) Frequency of major immune cell types in the tumor microenvironment was measured by flow cytometry (non-responders, n = 6; responders, n = 5/group). Data are presented as mean ± SEM. Statistical significance was determined using a two-tailed Student's *t*-test, and ANOVA with Tukey's post-test was performed for multiple comparisons. Data shown are representative of three independent experiments performed. $^{**}p < 0.01$; $^{***}p < 0.001$.

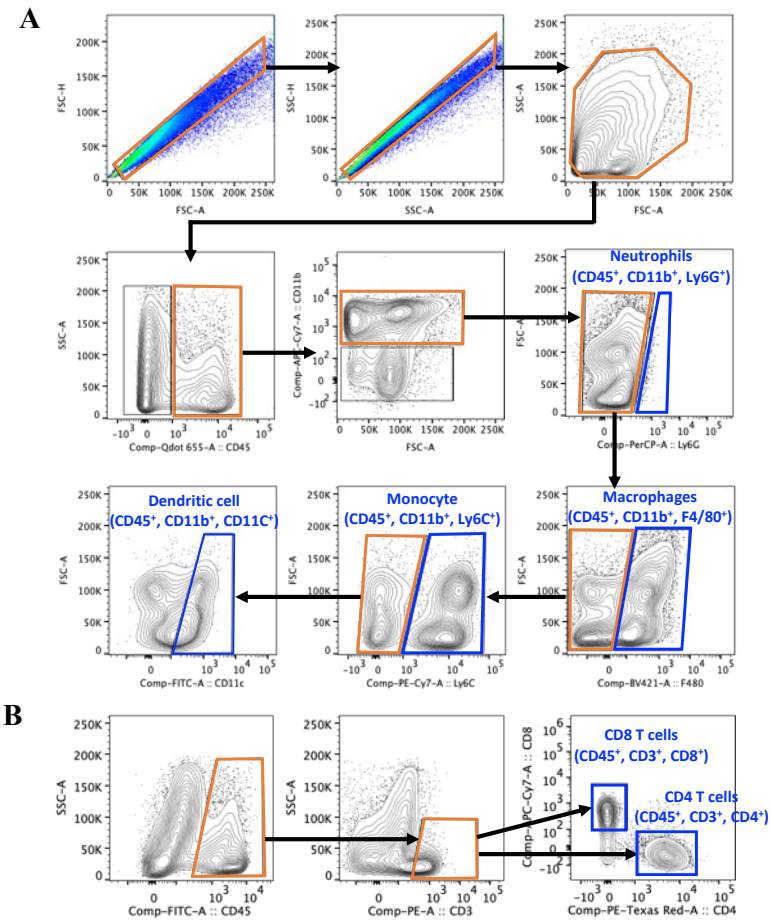

Figure 6. The gating strategy used to identify the different immune cell populations in the tumor. Immune cell populations were first gated based on the FSC-H and FSC-A, and SSA-H and SSC-A for single cell. After then, FSC-A and SSC-A positive portion were further gated based on CD45 expression. The subpopulations of the myeloid cells **(A)** and T cells **(B)** were gated based on specific surface markers as indicated in the panel.

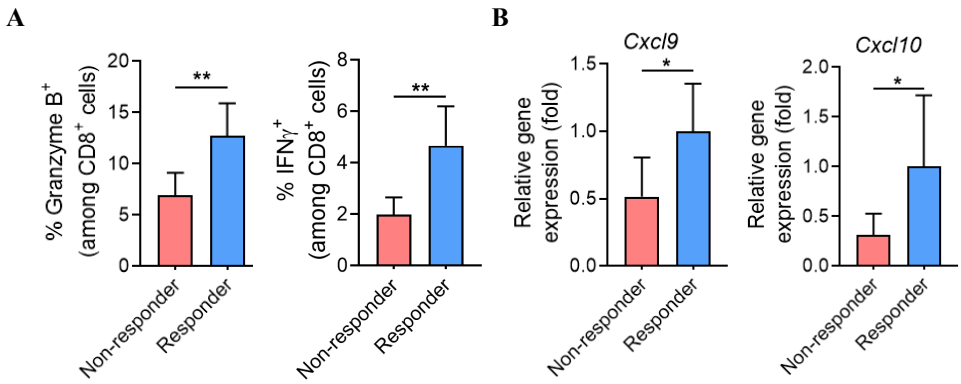

Figure 7. Increased cytotoxic T cell infiltration via up-regulation of chemo-attractants in responder to anti-PD1 treatment. (**A**) Population percentages of Granzyme B^+ and IFNγ^+ in tumor infiltrating $CD8^+$ T cells as determined by flow cytometry (n = 6/group). (**B**) Relative mRNA expression of *Cxcl9* and *Cxcl10* in tumors of non-responders and responders (n = 6/group). Data are presented as mean ± SEM. Statistical significance was determined using a two-tailed Student's *t*-test. Data shown are representative of three independent experiments performed. *$p < 0.05$; **$p < 0.01$.

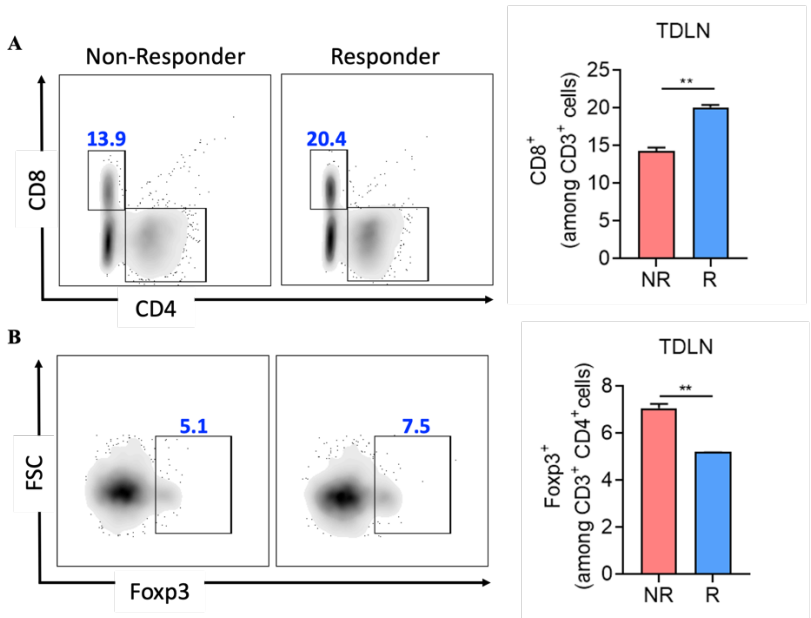

Figure 8. T cell changes in TdLNs to anti-PD1 treatment. (**A**) Population percentages of $CD8^+$ T cells in the TdLN as determined by flow cytometry (non-responders, n = 4; responders, n = 2/group). (**B**) Population percentages of $FoxP3^+$, $CD4^+$ T cells in the TdLN as determined by flow cytometry (non-responders, n = 4; responders, n = 2/group). Data are presented as mean ± SEM. Statistical significance was determined using a two-tailed Student's *t*-test. Data shown are representative of three independent experiments performed. $^{**}p < 0.01$.

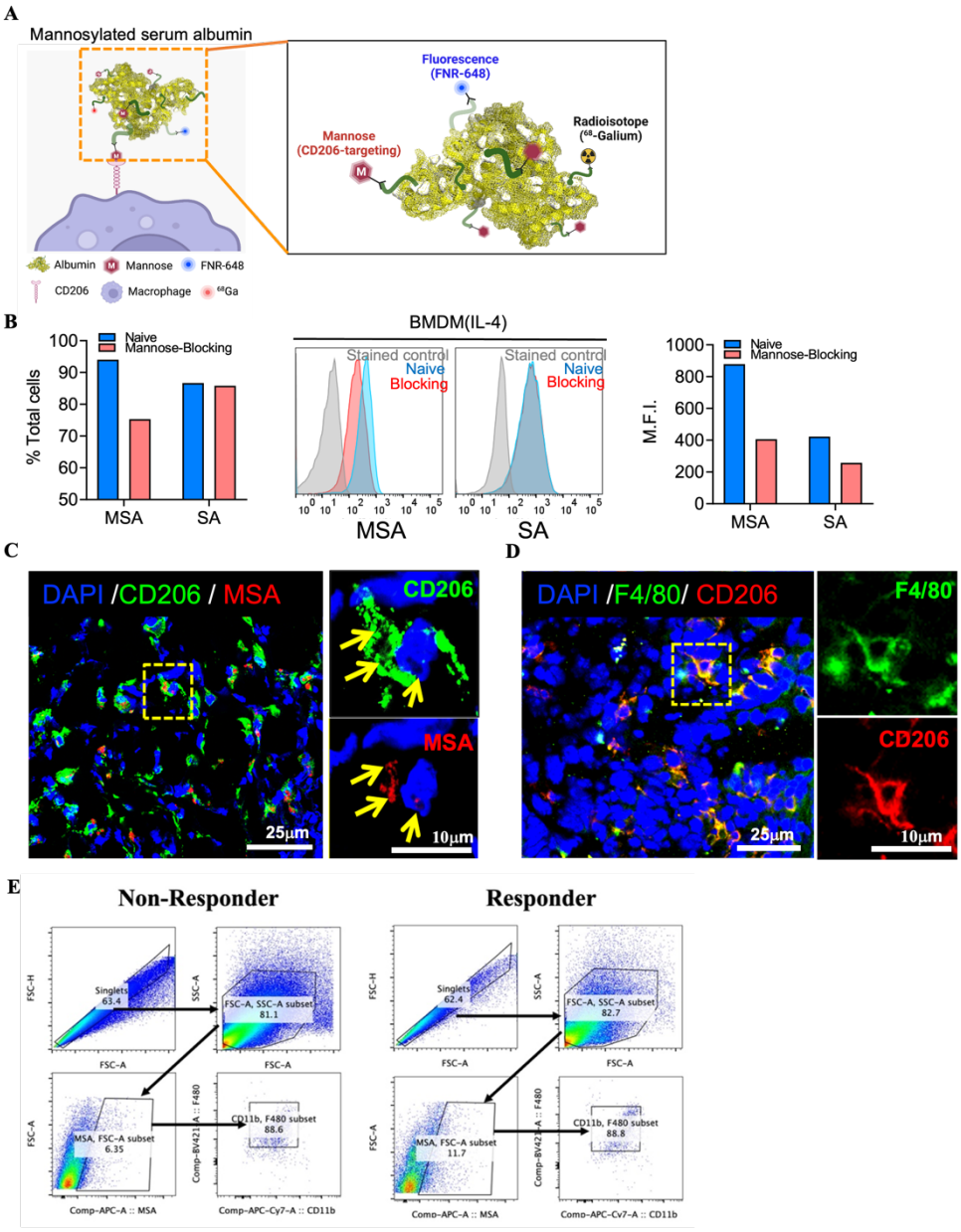
A
Mannosylated serum albumin
Fluorescence
(FNR-648)
Mannose
(CD206-targeting)
Radioisotope
(68-Galium)
Albumin
Mannose
FNR-648
CD206
Macrophage
68Ga
B
Naive
Mannose-Blocking
% Total cells
MSA
SA
BMDM(IL-4)
Stained control
Naive
Blocking
M.F.I.
C
DAPI /CD206 / MSA
CD206
MSA
25μm
10μm
D
DAPI /F4/80/ CD206
F4/80
CD206
25μm
10μm
E
Non-Responder
Responder
Singlets
FSC-A, SSC-A subset
MSA, FSC-A subset
CD11b, F480 subset
Comp-APC-A :: MSA
Comp-APC-Cy7-A :: CD11b

Figure 9. CD206 expressing cells-specific uptake of MSA. (A) Schematic illustration of MSA. **(B)** Flow cytometry analysis of CD206-targeted MSA incubated with IL-4 treated bone marrow derived- macrophages. **(C)** Representative immunofluorescence staining of CD206 (green) and MSA (red) in the tumor tissues. **(D)** Representative immunofluorescence staining of F4/80 (green) and CD206 (red) in the tumor tissues. **(E)** CD11b and F4/80 expression in MSA^+ cells after anti-PD1 treatment.

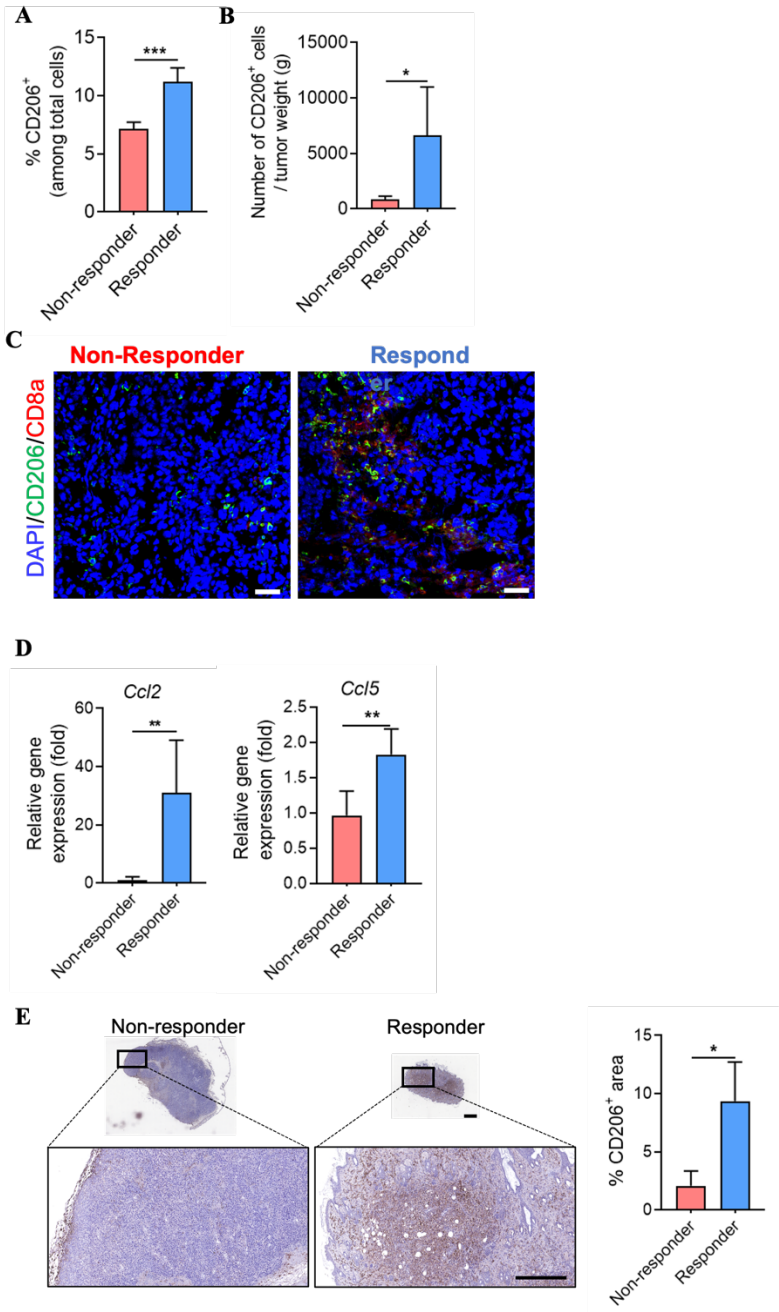

Figure 10. Significantly higher infiltration of CD206$^+$ macrophages in the tumor core in Responders. (A) Flow cytometry for the frequency of CD206$^+$ cells in non-responder and responder tumors (non-responders, n = 6; responders, n = 5/group). **(B)** The number of CD206$^+$ cells normalized to tumor weight. **(C)** Representative

immunofluorescence staining of CD206 (green) and CD8 (red) in the tumor tissues. Scale bar, 50 μm. Images are representative of two independent experiments. (**D**) Relative mRNA expression of *Ccl2* and *Ccl5* in tumors of non-responders and responders (n = 3/group). (**E**) Quantification of CD206 immunohistochemistry-stained tumor tissues from non-responders and responders. Scale bar, 1 mm. for upper images and 300 μm for magnified images. Data are presented as mean ± SEM. Statistical significance was determined using a two-tailed Student's *t*-test, and ANOVA with Tukey's post-test was performed for multiple comparisons. Data shown are representative of three independent experiments performed. *$p < 0.05$; **$p < 0.01$; ***$p < 0.001$.

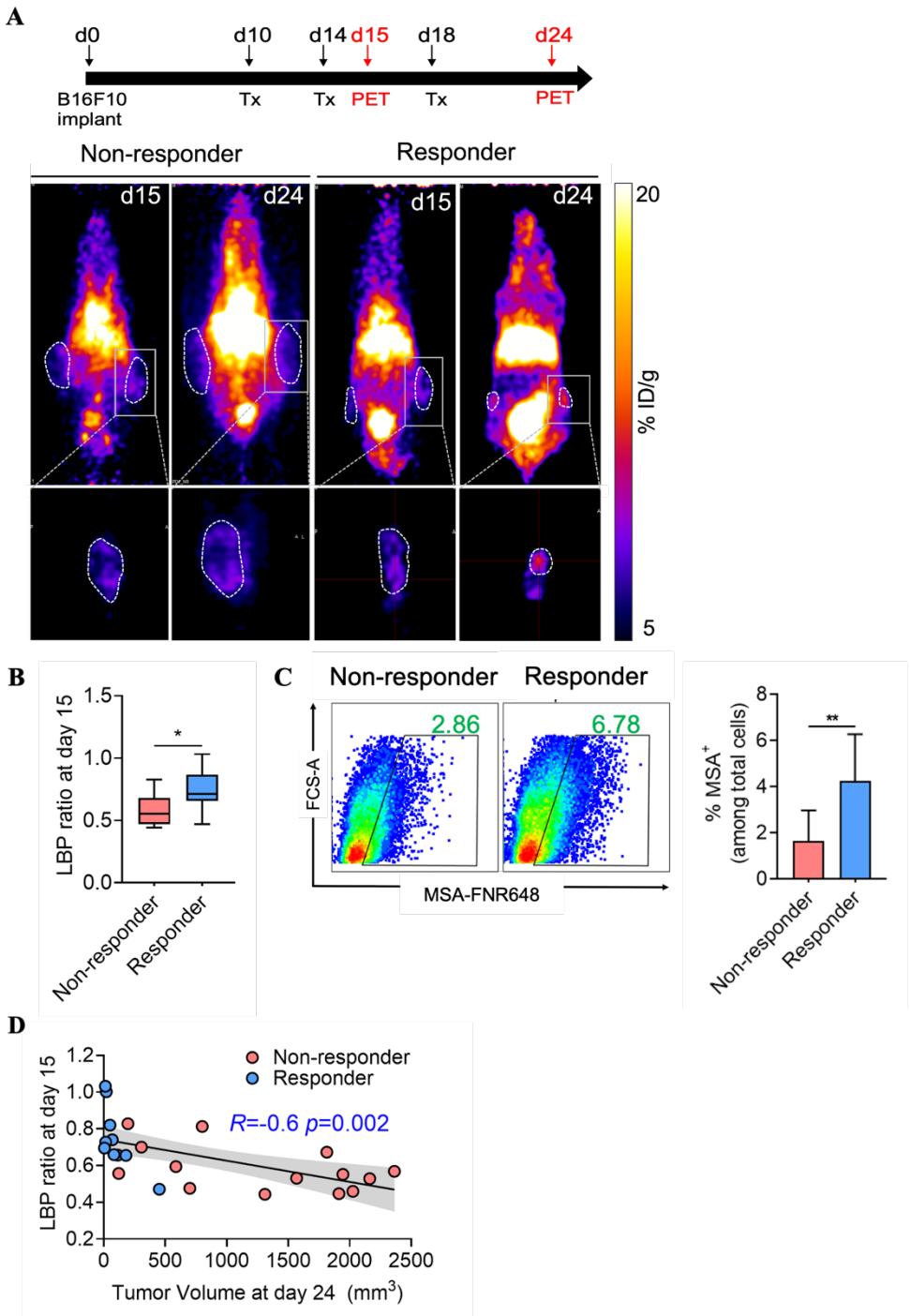

Figure 11. ***In vivo*** **imaging of anti-PD1 treated tumor using [^{68}Ga]Ga-MSA for CD206 targeted imaging in a murine model of melanoma.** (**A**) Overview of experimental representative PET images of B16F10-bearing mice that responded or

failed to respond to anti-PD1 treatment. Panels below the whole-body PET images are sagittal sections of the tumors to better visualize the PET signal status of MSA-positive cells. The scale bar of the image was adjusted for the image of the tumor site. The counts were corrected for radioisotope decay and thereafter normalized as % ID. At this time, the unit of the scale bar was configured to be the same in all images, and the lower limit was adjusted to 5 % ID/g to obtain an image from which the background signal was removed. (**B**) Measurement of Lesion to Blood pool (LBP) ratio at day 15 in the anti-PD1 treated tumor (non-responders, n = 14; responders, n = 10). (**C**) Representative flow cytometric dot plot (left) and percentages of MSA^+ cells as determined by flow cytometry (right) (non-responders, n = 9; responders, n = 7). (**D**) Parametric linear correlation between LBP (day 15) and tumor volume (day 24) (non-responders, n = 14, responders n = 10).

Data are presented as mean ± SEM. Statistical significance was determined using the two-tailed Student's *t*-test. Data shown are representative of two independent experiments performed. *$p < 0.05$; **$p < 0.01$.

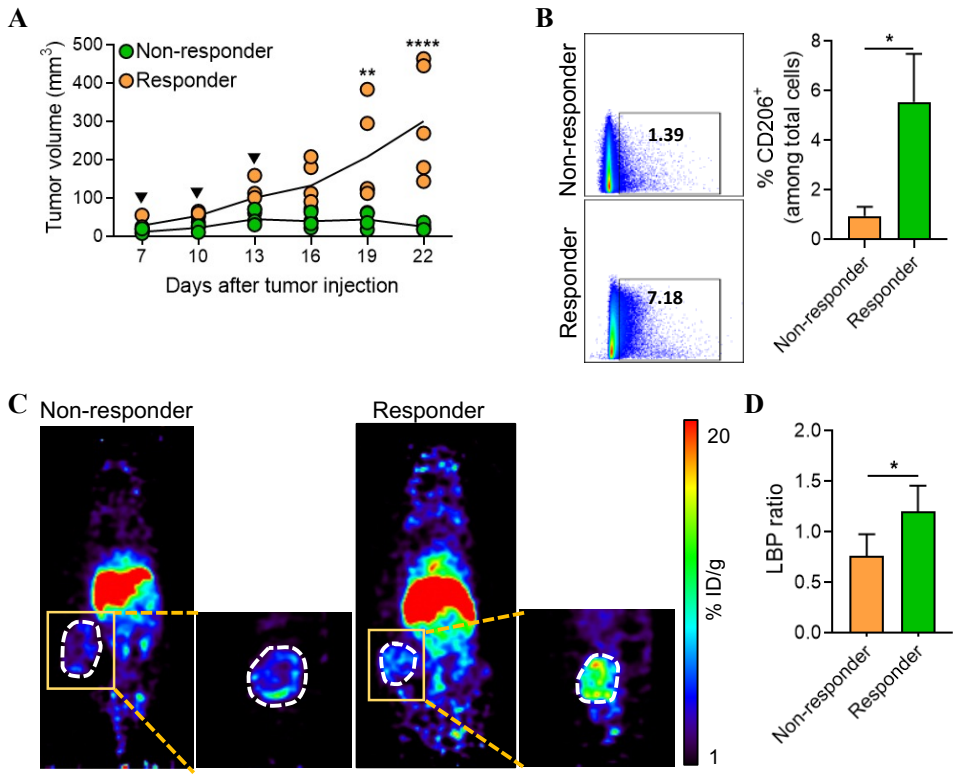

Figure 12. *In vivo* imaging of [^{68}Ga]Ga-MSA for CD206 targeted imaging in a murine model of colon adenocarcinoma. MC38 tumor-bearing mice were treated with 100 μg of anti-PD1(▼) on day 7, day 10, and day 13. Experiments were conducted 15 d after initiating the anti-PD1 treatment. **(A)** MC38 tumor volumes in mice treated with anti-PD1 (non-responders, n = 5; responders, n = 4). **(B)** Flow cytometry for the frequency of CD206$^+$ cells in non-responder and responder tumors (non-responders, n = 5; responders, n = 4). **(C)** Overview of experimental representative PET images of MC38-bearing mice that responded or failed to respond to anti-PD1 treatment. Panels next to the whole-body PET images are sagittal sections of the tumors to better visualize the PET signal status of MSA-positive cells. The scale bar of the image was adjusted for the image of the tumor site. The counts were corrected for radioisotope decay and thereafter normalized as %

ID. At this time, the unit of the scale bar was configured to be the same in all images, and the lower limit was adjusted to 1 % ID/g to obtain an image from which the background signal was removed. (**D**) Measurement of Lesion to Blood pool (LBP) ratio at day 22 in the anti-PD1 treated tumor (non-responders, n = 5; responders, n = 4). Data are presented as mean ± SEM. Statistical significance was determined using the two-tailed Student's *t*-test. Data shown are representative of two independent experiments performed. *$p < 0.05$; **$p < 0.01$; ****$p < 0.0001$.

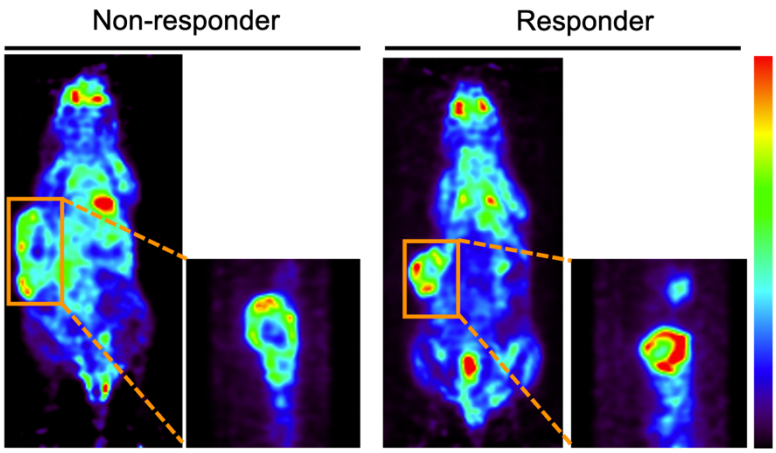

Figure 13. Similar pattern of [^{18}F]-FDG PET imaging in a murine model of melanoma. MC38 tumor-bearing mice were treated with 100 μg of anti-PD1(▼) on day 7, day 10, and day 13. Experiments were conducted 15 d after initiating the anti-PD1 treatment. Experimental representative PET images of MC38-bearing mice that responded or failed to respond to anti-PD1 treatment. Panels next to the whole-body PET images are sagittal sections of the tumors to better visualize the PET signal status.

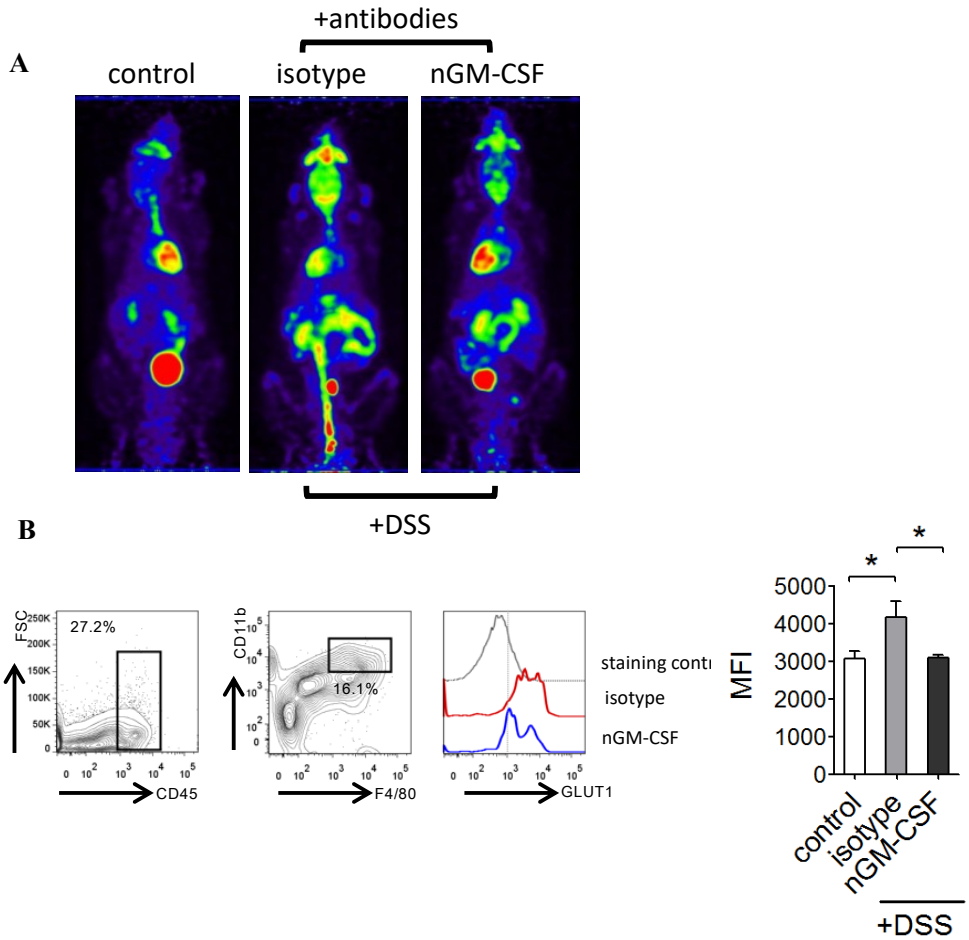

Figure 14. [^{18}F]-FDG PET imaging in ccolitis model. (A) C57BL/6J mice were provided water containing 3% DSS to induces colitis. Anti–GM-CSF or corresponding isotype Abs (50 μg per mouse) were injected i.p. at day 4. [18F]-FDG PET imaging was obtained after 48 h of Ab injection. Experimental representative Whole-body PET images. **(B)** Lamina propria single cells were isolated from col ons and analyzed by flow cytometry. Macrophages were gated for the $CD45^{+}F4/80^{+}CD11b^{+}$ population, and the expressions of GLUT-1 are displayed as hist ograms. Mean fluorescence intensity (MFI) of GLUT-1 signals was quantified and displayed in the right graph. Data are presented as mean ± SEM. Statistical

significance was determined using the two-tailed Student's *t*-test. Data shown are representative of two independent experiments performed. *$p < 0.05$.

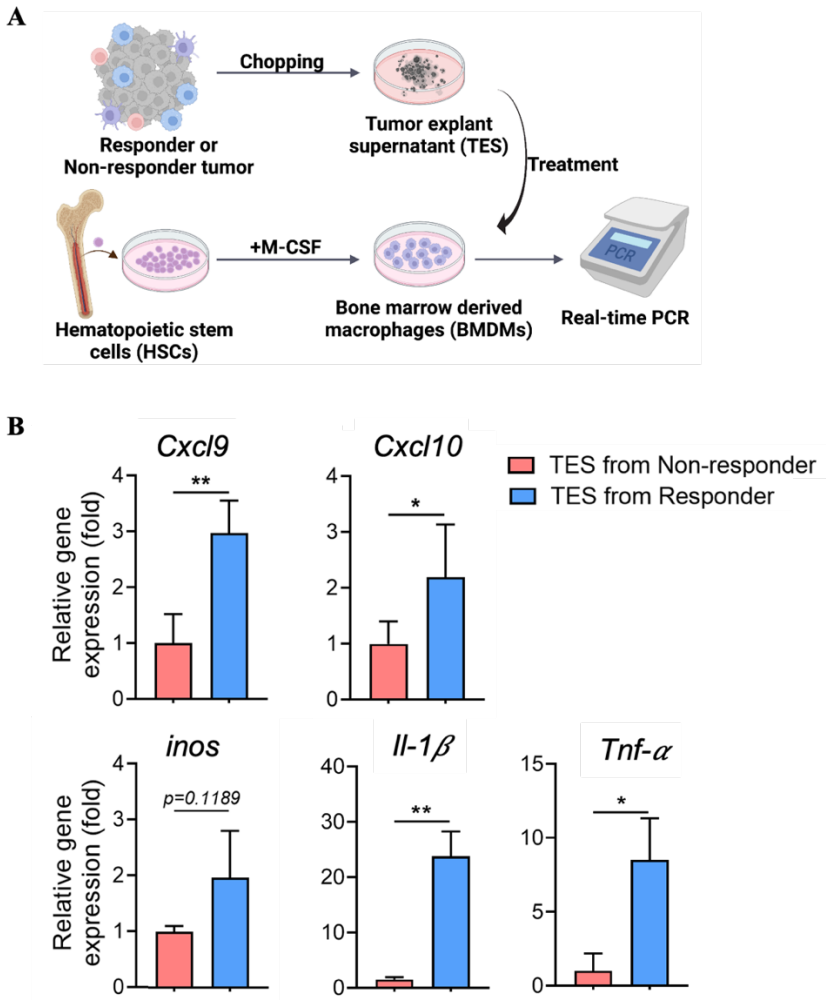

Figure 15. The TME altered by anti-PD1 treatment allows macrophages to modulate CD8$^+$ T cells immune response. (A) Schematic overview of the experimental design. (**B**) Relative mRNA expression of *Cxcl9, Cxcl10, inos, Il-1β* and *Tnf-α* in bone marrow-derived macrophages (BMDMs) treated with tumor explant supernatant (TES) obtained from tumors of non-responders or responders for 24 h (Isotype, Non-responder, n = 3; Responder, n=1). Data are presented as mean ± SEM. Statistical significance was determined using the two-tailed Student's *t*-test.

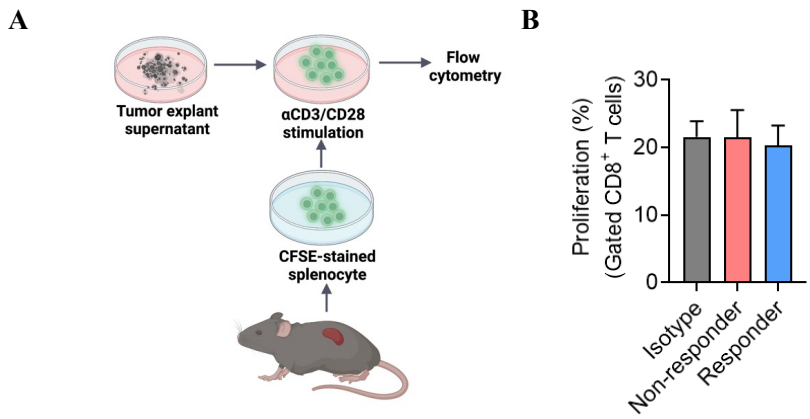

Figure 16. The TME altered by anti-PD1 treatment does not directly affect CD8$^+$ T cells immune response. (A) Schematic illustration of the experimental design for the T cell proliferation assay upon treatment with tumor explant supernatant (TES). **(B)** Proliferation of activated CD8$^+$ T cells exposed to TES in isotype, non-responder, or responder tumors (n = 3 / group). All data represented as mean ± S.E.M. Statistical significance was determined by two-way ANOVA.

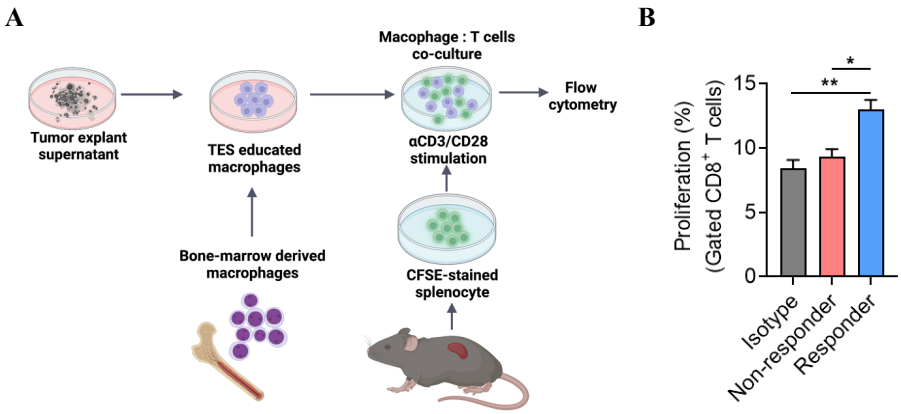

Figure 17. The TME-educated macrophages regulate the CD8$^+$ T cells immune response. (A) Schematic illustration of the experimental design for the T cell proliferation assay after co-culture with macrophages at a ratio of 4:1. (B) Proliferation of activated CD8$^+$ T cells in co-culture with TES educated (n = 3/ group). All data represented as mean ± S.E.M. Statistical significance was determined by two-way ANOVA. *$p < 0.05$; **$p < 0.01$.

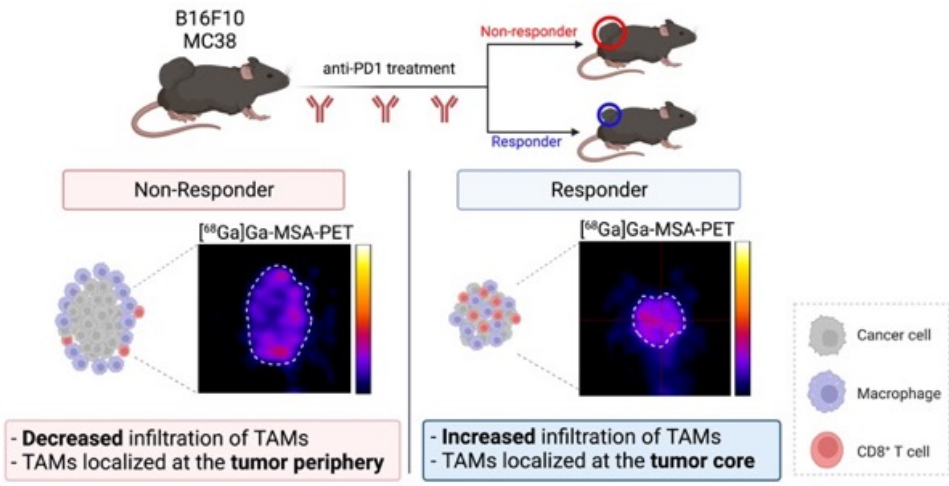

Figure 18. Schematic summary.

In responders using MSA imaging, augmented infiltration of TAMs was demonstrated after treatment with anti-PD1. There was a significant difference in TAMs localization, which moved to the core of the tumor in the responders after anti-PD1 treatment. The TME altered by anti-PD1 treatment induces a phenotypic change in TAMs to induce the infiltration and activation of $CD8^+$ T cells. As a result, Monitoring TAM enrichment using non-invasive MSA imaging could be used as a dynamic biomarker to evaluate the immune status of tumors after ICI treatment.

DISCUSSION

In this study, I first investigated the capability of non-invasive imaging of TAMs to evaluate responsiveness to anti-PD1 in a tumor-bearing mouse model.

Previous studies have shown how ICI therapy affects the dynamics of intratumoral $CD11b^+$ myeloid cells; this population comprises various immune cell types, MDSCs, neutrophils, and natural killer cells (NK cells) (39). As MDSCs represent an immunosuppressive phenotype and NK cells possess cytotoxic abilities similar to $CD8^+$ T cells, it is challenging to discern responders from non-responders to ICI treatment by monitoring the entire $CD11b^+$ population (40). Nonetheless, overall immune cell infiltration in the tumor microenvironment is a predictive factor for therapeutic efficacy (41, 42). Furthermore, my results showed that most of the TAMs produced by MSA showed a positive correlation with the therapeutic effect. Thus, my data are meaningful as the first non-invasive observation of dynamic changes in TAMs in response to ICI therapy.

To investigate whether overall macrophage enrichment could predict responsiveness to ICIs, I used MSA to monitor macrophages by targeting the mannose receptor after anti-PD1 treatment. CD206 is generally known as the M2 marker (43-45). However, increasing evidence suggests that this dualistic classification does not address the complex heterogeneity of macrophages, emphasizing the importance of unbiasedly describing the functions instead of the putative M1/M2 phenotypes (46, 47). Further, I confirmed that the expression of MHCII and iNOS, which induce T cell activation, was increased in TAMs from responders, regardless of CD206 expression. Therefore, I suggest that the pro- or

anti-tumoral macrophages should be defined by specific activities rather than expressing markers. From this viewpoint, targeting $CD206^{+}$ macrophages was interpreted as TAMs in this experiment. In summary, the expression of CD206 cannot explain the functional state of TAMs; however, I only assessed the progression of anti-tumor responses to anti-PD-1 treatment through MSA imaging.

The CD206 consists of a cysteine-rich region, a fibronectin type II domain, eight C-type lectin-like domains (CTLDs), a transmembrane region, and a short cytosolic tail (48). CD206 is known to be controlled by various cytokine (IL-10, IL-4, IL-13 and IFN-γ), prostaglandins, LPS and the transcription factor PPAR-γ (49-52). CD206 is known to corelate with various inflammatory disease (53). Especially, CD206 is involved in the activation and inflammation of macrophages, suggesting that inflammatory reactions after anti-PD1 treatment may induce the expression of CD206. In addition, referring to the study of Jaynes et al., they also found that CD206 expressing TAM in the tumor was also have inflammatory phenotype by producing inflammatory cytokines such as TNF-α and IL-1(47). Moreover, Zhou et al. also confirmed that CD206 expressing TAMs had an anti-tumoral effect (46). To summarize the studies, TAM, which infiltrated tumor after anti-cancer drug, has an anti-tumoral character while expressing CD206. The inducer of CD206 is various factor which induced by cancer cells and immune reaction mediated factors present in the cancer.

Monitoring TAM enrichment using non-invasive imaging could be used as a biomarker to evaluate the dynamic immune status of tumors. As immune status changes dynamically according to tumor progression and treatment, monitoring the tumor immune microenvironment could be important for using immune-oncology

drugs. Conventional imaging, including CT and fluorodeoxyglucose PET, cannot differentiate between cancer and immune cells in the tumor microenvironment. Further, increased immune cells are a good predictive dynamic biomarker considering the mechanism of action of immuno-oncology drugs. Therefore, direct monitoring of immune cells using non-invasive imaging is promising for evaluating the responsiveness of ICIs in the early phase. These novel imaging methods, including [^{68}Ga]Ga-MSA, could provide dynamic biomarkers reflecting the mechanisms of immune-oncology drugs.

TAMs exhibit distinct characteristics depending on their localization within the tumor core (54, 55). Peripheral TAMs showed a more mature suppressive phenotype than those in the tumor core. Although the functional characteristics of TAMs involved in response to anti-PD1 remain to be elucidated, I confirmed that TAMs moved to the tumor core in the responder group after anti-PD1 treatment. Tumors with pre-existing and homogeneously distributed $CD8^+$ T cells at diagnosis are more likely to respond to ICI treatment. In contrast, tumors with a heterogeneous $CD8^+$ T cell distribution show a weaker response (56). As shown in previous research, TAMs induce impeding of T cells to inhibit the response to anti-PD1. The results of TAM localization can be interpreted as the induction of an immune response to stimulate the infiltration of T cells after ICI treatment.

To obtain a more variable response, I modified the amount of anti-PD1. This is because the significant difference in regional DNA content, which was confirmed using whole-genome array, even though it is an inbred mice (57). These differences can contribute to pathological susceptibility. In addition, Sine there is a heterogeneity in the cancer cell line due to diverse biological processes, including senescence,

stress and cell cycle, and mutation; immunotherapy's responsiveness appears in various ways (23, 58).

Overall, developing improved methods to monitor therapeutic responses can provide patients resistant to ICI therapy with the opportunity to receive other treatments. In conclusion, this study presents a method for non-invasively identification of the number and location of TAMs as a factor in confirming the change and activity of immune cells after ICI treatment.

REFERENCE

1. Sharma P, Allison JP. The Future of Immune Checkpoint Therapy. *Science* (2015) 348(6230):56-61. doi: 10.1126/science.aaa8172.
2. Sharma P, Hu-Lieskovan S, Wargo JA, Ribas A. Primary, Adaptive, and Acquired Resistance to Cancer Immunotherapy. *Cell* (2017) 168(4):707-23. doi: 10.1016/j.cell.2017.01.017.
3. Antonios JP, Soto H, Everson RG, Moughon DL, Wang AC, Orpilla J, et al. Detection of Immune Responses after Immunotherapy in Glioblastoma Using Pet and Mri. *Proc Natl Acad Sci U S A* (2017) 114(38):10220-5. Epub 20170905. doi: 10.1073/pnas.1706689114.
4. Borcoman E, Nandikolla A, Long G, Goel S, Le Tourneau C. Patterns of Response and Progression to Immunotherapy. *Am Soc Clin Oncol Educ Book* (2018) 38:169-78. doi: 10.1200/EDBK_200643.
5. Persigehl T, Lennartz S, Schwartz LH. Irecist: How to Do It. *Cancer Imaging* (2020) 20(1):2. doi: 10.1186/s40644-019-0281-x.
6. Guillerey C, Huntington ND, Smyth MJ. Targeting Natural Killer Cells in Cancer Immunotherapy. *Nat Immunol* (2016) 17(9):1025-36. doi: 10.1038/ni.3518.
7. Waldman AD, Fritz JM, Lenardo MJ. A Guide to Cancer Immunotherapy: From T Cell Basic Science to Clinical Practice. *Nat Rev Immunol* (2020) 20(11):651-68. Epub 20200520. doi: 10.1038/s41577-020-0306-5.
8. Larimer BM, Wehrenberg-Klee E, Dubois F, Mehta A, Kalomeris T, Flaherty K, et al. Granzyme B Pet Imaging as a Predictive Biomarker of Immunotherapy Response. *Cancer Research* (2017) 77(9):2318-27. doi: 10.1158/0008-5472.CAN-16-3346.
9. LaSalle T, Austin EE, Rigney G, Wehrenberg-Klee E, Nesti S, Larimer B, et al. Granzyme B Pet Imaging of Immune-Mediated Tumor Killing as a Tool for Understanding Immunotherapy Response. *J Immunother Cancer* (2020) 8(1). doi: 10.1136/jitc-2019-000291.
10. Kristensen LK, Fröhlich C, Christensen C, Melander MC, Poulsen TT, Galler GR, et al. Cd4(+) and Cd8a(+) Pet Imaging Predicts Response to Novel Pd-1 Checkpoint Inhibitor: Studies of Sym021 in Syngeneic Mouse Cancer Models. *Theranostics* (2019) 9(26):8221-38. Epub 20191018. doi: 10.7150/thno.37513.
11. Gibson HM, McKnight BN, Malysa A, Dyson G, Wiesend WN, McCarthy CE, et al. Ifnγ Pet Imaging as a Predictive Tool for Monitoring Response to Tumor Immunotherapy. *Cancer research* (2018) 78(19):5706-17. Epub 2018/08/16. doi: 10.1158/0008-5472.CAN-18-0253.
12. Xiao Z, Pure E. Imaging of T-Cell Responses in the Context of Cancer Immunotherapy. *Cancer Immunol Res* (2021) 9(5):490-502. doi: 10.1158/2326-6066.CIR-20-0678.
13. Manafi-Farid R, Ataeinia B, Ranjbar S, Jamshidi Araghi Z, Moradi MM, Pirich C, et al. Immunopet: Antibody-Based Pet Imaging in Solid Tumors. *Front Med (Lausanne)* (2022) 9:916693. Epub 20220628. doi:

10.3389/fmed.2022.916693.
14. DeNardo DG, Ruffell B. Macrophages as Regulators of Tumour Immunity and Immunotherapy. *Nat Rev Immunol* (2019) 19(6):369-82. doi: 10.1038/s41577-019-0127-6.
15. Gubin MM, Esaulova E, Ward JP, Malkova ON, Runci D, Wong P, et al. High-Dimensional Analysis Delineates Myeloid and Lymphoid Compartment Remodeling During Successful Immune-Checkpoint Cancer Therapy. *Cell* (2018) 175(4):1014-30.e19. doi: https://doi.org/10.1016/j.cell.2018.09.030.
16. Zhu Y, Knolhoff BL, Meyer MA, Nywening TM, West BL, Luo J, et al. Csf1/Csf1r Blockade Reprograms Tumor-Infiltrating Macrophages and Improves Response to T-Cell Checkpoint Immunotherapy in Pancreatic Cancer Models. *Cancer Res* (2014) 74(18):5057-69. Epub 20140731. doi: 10.1158/0008-5472.CAN-13-3723.
17. Sun J, Park C, Guenthner N, Gurley S, Zhang L, Lubben B, et al. Tumor-Associated Macrophages in Multiple Myeloma: Advances in Biology and Therapy. *J Immunother Cancer* (2022) 10(4). doi: 10.1136/jitc-2021-003975.
18. Ruffell B, Chang-Strachan D, Chan V, Rosenbusch A, Ho Christine MT, Pryer N, et al. Macrophage Il-10 Blocks Cd8+ T Cell-Dependent Responses to Chemotherapy by Suppressing Il-12 Expression in Intratumoral Dendritic Cells. *Cancer Cell* (2014) 26(5):623-37. doi: https://doi.org/10.1016/j.ccell.2014.09.006.
19. Pascual-Garcia M, Bonfill-Teixidor E, Planas-Rigol E, Rubio-Perez C, Iurlaro R, Arias A, et al. Lif Regulates Cxcl9 in Tumor-Associated Macrophages and Prevents Cd8(+) T Cell Tumor-Infiltration Impairing Anti-Pd1 Therapy. *Nat Commun* (2019) 10(1):2416. Epub 20190611. doi: 10.1038/s41467-019-10369-9.
20. Kato S, Okamura R, Kumaki Y, Ikeda S, Nikanjam M, Eskander R, et al. Expression of Tim3/Vista Checkpoints and the Cd68 Macrophage-Associated Marker Correlates with Anti-Pd1/Pdl1 Resistance: Implications of Immunogram Heterogeneity. *Oncoimmunology* (2020) 9(1):1708065. Epub 20200217. doi: 10.1080/2162402X.2019.1708065.
21. Arlauckas SP, Garris CS, Kohler RH, Kitaoka M, Cuccarese MF, Yang KS, et al. In Vivo Imaging Reveals a Tumor-Associated Macrophage-Mediated Resistance Pathway in Anti-Pd-1 Therapy. *Sci Transl Med* (2017) 9(389). doi: 10.1126/scitranslmed.aal3604.
22. Gyori D, Lim EL, Grant FM, Spensberger D, Roychoudhuri R, Shuttleworth SJ, et al. Compensation between Csf1r+ Macrophages and Foxp3+ Treg Cells Drives Resistance to Tumor Immunotherapy. *JCI Insight* (2018) 3(11). Epub 20180607. doi: 10.1172/jci.insight.120631.
23. Qu Y, Wen J, Thomas G, Yang W, Prior W, He W, et al. Baseline Frequency of Inflammatory Cxcl9-Expressing Tumor-Associated Macrophages Predicts Response to Avelumab Treatment. *Cell Rep* (2020) 32(1):107873. doi: 10.1016/j.celrep.2020.107873.
24. Obenauf AC, Zou Y, Ji AL, Vanharanta S, Shu W, Shi H, et al. Therapy-Induced Tumour Secretomes Promote Resistance and Tumour

Progression. *Nature* (2015) 520(7547):368-72. Epub 20150325. doi: 10.1038/nature14336.
25. Yoshimura T. The Chemokine Mcp-1 (Ccl2) in the Host Interaction with Cancer: A Foe or Ally? *Cell Mol Immunol* (2018) 15(4):335-45. Epub 20180129. doi: 10.1038/cmi.2017.135.
26. Dijkgraaf EM, Heusinkveld M, Tummers B, Vogelpoel LT, Goedemans R, Jha V, et al. Chemotherapy Alters Monocyte Differentiation to Favor Generation of Cancer-Supporting M2 Macrophages in the Tumor Microenvironment. *Cancer Res* (2013) 73(8):2480-92. Epub 20130222. doi: 10.1158/0008-5472.CAN-12-3542.
27. Fu XT, Song K, Zhou J, Shi YH, Liu WR, Shi GM, et al. Tumor-Associated Macrophages Modulate Resistance to Oxaliplatin Via Inducing Autophagy in Hepatocellular Carcinoma. *Cancer Cell Int* (2019) 19:71. Epub 20190325. doi: 10.1186/s12935-019-0771-8.
28. Choi JY, Jeong JM, Yoo BC, Kim K, Kim Y, Yang BY, et al. Development of 68ga-Labeled Mannosylated Human Serum Albumin (Msa) as a Lymph Node Imaging Agent for Positron Emission Tomography. *Nucl Med Biol* (2011) 38(3):371-9. Epub 20101203. doi: 10.1016/j.nucmedbio.2010.09.010.
29. Park JB, Suh M, Park JY, Park JK, Kim YI, Kim H, et al. Assessment of Inflammation in Pulmonary Artery Hypertension by (68)Ga-Mannosylated Human Serum Albumin. *Am J Respir Crit Care Med* (2020) 201(1):95-106. doi: 10.1164/rccm.201903-0639OC.
30. Lee S-P, Im H-J, Kang S, Chung S-J, Cho YS, Kang H, et al. Noninvasive Imaging of Myocardial Inflammation in Myocarditis Using (68)Ga-Tagged Mannosylated Human Serum Albumin Positron Emission Tomography. *Theranostics* (2017) 7(2):413-24. doi: 10.7150/thno.15712.
31. Gao H, Korn JM, Ferretti S, Monahan JE, Wang Y, Singh M, et al. High-Throughput Screening Using Patient-Derived Tumor Xenografts to Predict Clinical Trial Drug Response. *Nat Med* (2015) 21(11):1318-25. Epub 20151019. doi: 10.1038/nm.3954.
32. Aslan K, Turco V, Blobner J, Sonner JK, Liuzzi AR, Nunez NG, et al. Heterogeneity of Response to Immune Checkpoint Blockade in Hypermutated Experimental Gliomas. *Nat Commun* (2020) 11(1):931. Epub 20200218. doi: 10.1038/s41467-020-14642-0.
33. Tokunaga R, Zhang W, Naseem M, Puccini A, Berger MD, Soni S, et al. Cxcl9, Cxcl10, Cxcl11/Cxcr3 Axis for Immune Activation - a Target for Novel Cancer Therapy. *Cancer Treat Rev* (2018) 63:40-7. Epub 20171126. doi: 10.1016/j.ctrv.2017.11.007.
34. Chung H, Park JY, Kim K, Yoo RJ, Suh M, Gu GJ, et al. Circulation Time-Optimized Albumin Nanoplatform for Quantitative Visualization of Lung Metastasis Via Targeting of Macrophages. *ACS Nano* (2022). Epub 20220809. doi: 10.1021/acsnano.2c03075.
35. Na YR, Gu GJ, Jung D, Kim YW, Na J, Woo JS, et al. Correction: Gm-Csf Induces Inflammatory Macrophages by Regulating Glycolysis and Lipid Metabolism. *J Immunol* (2017) 198(7):3000. doi: 10.4049/jimmunol.1700174.
36. House IG, Savas P, Lai J, Chen AXY, Oliver AJ, Teo ZL, et al.

Macrophage-Derived Cxcl9 and Cxcl10 Are Required for Antitumor Immune Responses Following Immune Checkpoint Blockade. *Clin Cancer Res* (2020) 26(2):487-504. Epub 20191021. doi: 10.1158/1078-0432.Ccr-19-1868.
37. Klug F, Prakash H, Huber PE, Seibel T, Bender N, Halama N, et al. Low-Dose Irradiation Programs Macrophage Differentiation to an Inos(+)/M1 Phenotype That Orchestrates Effective T Cell Immunotherapy. *Cancer Cell* (2013) 24(5):589-602. Epub 20131024. doi: 10.1016/j.ccr.2013.09.014.
38. Pascual-García M, Bonfill-Teixidor E, Planas-Rigol E, Rubio-Perez C, Iurlaro R, Arias A, et al. Lif Regulates Cxcl9 in Tumor-Associated Macrophages and Prevents Cd8(+) T Cell Tumor-Infiltration Impairing Anti-Pd1 Therapy. *Nat Commun* (2019) 10(1):2416. Epub 20190611. doi: 10.1038/s41467-019-10369-9.
39. Rashidian M, LaFleur MW, Verschoor VL, Dongre A, Zhang Y, Nguyen TH, et al. Immuno-Pet Identifies the Myeloid Compartment as a Key Contributor to the Outcome of the Antitumor Response under Pd-1 Blockade. *Proc Natl Acad Sci U S A* (2019) 116(34):16971-80. Epub 20190802. doi: 10.1073/pnas.1905005116.
40. Theivanthiran B, Evans KS, DeVito NC, Plebanek M, Sturdivant M, Wachsmuth LP, et al. A Tumor-Intrinsic Pd-L1/Nlrp3 Inflammasome Signaling Pathway Drives Resistance to Anti-Pd-1 Immunotherapy. *J Clin Invest* (2020) 130(5):2570-86. doi: 10.1172/JCI133055.
41. Bruni D, Angell HK, Galon J. The Immune Contexture and Immunoscore in Cancer Prognosis and Therapeutic Efficacy. *Nat Rev Cancer* (2020) 20(11):662-80. Epub 20200804. doi: 10.1038/s41568-020-0285-7.
42. Tavaré R, Danton M, Giurleo JT, Makonnen S, Hickey C, Arnold TC, et al. Immuno-Pet Monitoring of Lymphocytes Using the Cd8-Specific Antibody Regn5054. *Cancer Immunol Res* (2022). Epub 20220727. doi: 10.1158/2326-6066.Cir-21-0405.
43. Murray PJ, Allen JE, Biswas SK, Fisher EA, Gilroy DW, Goerdt S, et al. Macrophage Activation and Polarization: Nomenclature and Experimental Guidelines. *Immunity* (2014) 41(1):14-20. doi: 10.1016/j.immuni.2014.06.008.
44. Mosser DM, Edwards JP. Exploring the Full Spectrum of Macrophage Activation. *Nat Rev Immunol* (2008) 8(12):958-69. doi: 10.1038/nri2448.
45. Li Y, Wu H, Ji B, Qian W, Xia S, Wang L, et al. Targeted Imaging of Cd206 Expressing Tumor-Associated M2-Like Macrophages Using Mannose-Conjugated Antibiofouling Magnetic Iron Oxide Nanoparticles. *ACS Appl Bio Mater* (2020) 3(7):4335-47. Epub 20200611. doi: 10.1021/acsabm.0c00368.
46. Zhou X, Liu Y, Hu M, Wang M, Liu X, Huang L. Relaxin Gene Delivery Modulates Macrophages to Resolve Cancer Fibrosis and Synergizes with Immune Checkpoint Blockade Therapy. *Sci Adv* (2021) 7(8). Epub 20210217. doi: 10.1126/sciadv.abb6596.
47. Jaynes JM, Sable R, Ronzetti M, Bautista W, Knotts Z, Abisoye-Ogunniyan A, et al. Mannose Receptor (Cd206) Activation in Tumor-Associated Macrophages Enhances Adaptive and Innate Antitumor Immune Responses. *Sci Transl Med* (2020) 12(530). doi: 10.1126/scitranslmed.aax6337.

48. Martinez-Pomares L. The Mannose Receptor. *J Leukoc Biol* (2012) 92(6):1177-86. Epub 20120910. doi: 10.1189/jlb.0512231.
49. Schreiber S, Blum JS, Chappel JC, Stenson WF, Stahl PD, Teitelbaum SL, et al. Prostaglandin E Specifically Upregulates the Expression of the Mannose-Receptor on Mouse Bone Marrow-Derived Macrophages. *Cell Regul* (1990) 1(5):403-13. doi: 10.1091/mbc.1.5.403.
50. Shepherd VL, Abdolrasulnia R, Garrett M, Cowan HB. Down-Regulation of Mannose Receptor Activity in Macrophages after Treatment with Lipopolysaccharide and Phorbol Esters. *J Immunol* (1990) 145(5):1530-6.
51. Harris N, Super M, Rits M, Chang G, Ezekowitz RA. Characterization of the Murine Macrophage Mannose Receptor: Demonstration That the Downregulation of Receptor Expression Mediated by Interferon-Gamma Occurs at the Level of Transcription. *Blood* (1992) 80(9):2363-73.
52. Longoni D, Piemonti L, Bernasconi S, Mantovani A, Allavena P. Interleukin-10 Increases Mannose Receptor Expression and Endocytic Activity in Monocyte-Derived Dendritic Cells. *Int J Clin Lab Res* (1998) 28(3):162-9. doi: 10.1007/s005990050037.
53. Embgenbroich M, van der Zande HJP, Hussaarts L, Schulte-Schrepping J, Pelgrom LR, Garcia-Tardon N, et al. Soluble Mannose Receptor Induces Proinflammatory Macrophage Activation and Metaflammation. *Proc Natl Acad Sci U S A* (2021) 118(31). doi: 10.1073/pnas.2103304118.
54. Arlauckas SP, Garren SB, Garris CS, Kohler RH, Oh J, Pittet MJ, et al. Arg1 Expression Defines Immunosuppressive Subsets of Tumor-Associated Macrophages. *Theranostics* (2018) 8(21):5842-54. Epub 20181112. doi: 10.7150/thno.26888.
55. Huang Y-K, Wang M, Sun Y, Di Costanzo N, Mitchell C, Achuthan A, et al. Macrophage Spatial Heterogeneity in Gastric Cancer Defined by Multiplex Immunohistochemistry. *Nature Communications* (2019) 10(1):3928. doi: 10.1038/s41467-019-11788-4.
56. Waldman AD, Fritz JM, Lenardo MJ. A Guide to Cancer Immunotherapy: From T Cell Basic Science to Clinical Practice. *Nature Reviews Immunology* (2020) 20(11):651-68. doi: 10.1038/s41577-020-0306-5.
57. Li J, Jiang T, Mao JH, Balmain A, Peterson L, Harris C, et al. Genomic Segmental Polymorphisms in Inbred Mouse Strains. *Nat Genet* (2004) 36(9):952-4. Epub 20040822. doi: 10.1038/ng1417.
58. Gambardella G, Viscido G, Tumaini B, Isacchi A, Bosotti R, di Bernardo D. A Single-Cell Analysis of Breast Cancer Cell Lines to Study Tumour Heterogeneity and Drug Response. *Nat Commun* (2022) 13(1):1714. Epub 20220331. doi: 10.1038/s41467-022-29358-6.

국문 초록

면역 관문 억제제는 숙주 면역체계를 활성화시켜 향상된 자가면역력으로 암세포를 공격하도록 유도하는 항암제이다. 기존의 세포독성 항암제와는 다르게 직접적으로 암세포를 공격하지 않기 때문에 종양으로 몰려드는 면역세포로 인해 일시적으로 종양이 증가될 수 있어 종양크기의 변화만으로 효과를 결정하는 것은 부정확하다. 특히, 면역 관문 억제제에 대한 반응성을 종양의 크기만으로 확인하는데 상당히 오랜 시간이 소요되어 이미 반응성을 가지지 않는다는 것을 확인하면 대부분의 환자는 다른 치료법을 시도 할 수 없는 상태라는 큰 문제점이 있다. 따라서 종양 크기 외에 면역세포의 변화 등을 비 침습적으로 확인하고자 하는 연구들이 진행되고 있다.

본 연구에서는 종양 미세환경의 상당수를 차지하며 종양에서 다양한 역할을 하고 있다고 보고된 큰포식세포를 초타겟으ㄹ 하여 면역 관문 억제제에 대한 반응성을 확인하는 마커로써의 가능성을 검증하였다. 면역 관문 억제제 반응성군에서 종양내로 큰포식세포가 증가되는 것을 확인하였고, 증가된 큰포식세포의 대부분이 만노즈 수용체 (CD206) 를 발현하고 있는 것을 발견하여 이를 타겟팅 할 수 있는 나노복합체인 만노실화 알부민을 사용하여 비침습적으로 면역 관문 억제제에 대한 반응성을 확인하였다. 특히, 면역 관문 억제제 반응성군에서 만노즈 수용체를 발현하는 큰포식세포가 비반응성군보다 증가되어 있었으며, 종양 전반에 걸쳐 고르게 분포하는 것을 확인하였다. 또한 면역 관문 억제제의 직접

적인 표적세포인 T 세포에 대한 큰포식세포의 역할을 확인하기 위해서 종양 미세환경을 나타낼 수 있는 종양 삼출물을 획득하여 면역관문 억제제의 반응성에 따라서 큰포식세포가 T 세포의 활성화를 조절하는 것을 확인하였다.

본 연구를 통하여, 면역 관문 억제제의 반응성에 따라서 큰포식세포가 T 세포의 활성화 유도에 중요한 역할을 하는 것을 확인할 수 있었다. 또한 반응성에 따른 종양관련 큰포식세포의 비침습적 이미징은 면역관문 억제제에 대한 항-종양 반응의 진행을 추정하는데 도움이 될 수 있으며, 환자의 치료옵션에 대한 더 나은 결정을 할 수 있도록 도움을 줄 수 있음을 검증할 수 있었다.

Keywords : 큰포식세포, 만노즈 수용체, 만노실화 알부민, 면역 관문억제제, 양전자 방출 단층촬영

Student Number: 2015-30540